Doctoral Dissertation (Censored)
博士論文(要約)

Theoretical prediction of the phase transition route from β to λ phases of trititanium pentoxide

(五酸化三チタンにおけるβからλ相への相転移の理論予測)

A Dissertation Submitted for the Degree of Doctor of Philosophy
December 2021

令和3年12月博士(理学)申請

Department of Chemistry, Graduate School of Science,
The University of Tokyo

東京大学大学院理学系研究科

化学専攻

Takuma Takeda

武田　拓真

Abstract

Introduction

Five phases of trititanium pentaoxide Ti_3O_5, α, β, γ, δ and λ are reported up to now. Three of these five phases, α, λ and β phases have pseudobrookite-related structure, and λ and β-Ti_3O_5 have structural phase transition by kinds of external stimulation such as photo-inducing, temperature and pressure [1, 2]. It might be regarded that there is an arrangement of atomic coordination in four of eight inequivalent sites, Ti(3), O(3), O(4) and O(5) in the phase transition. However, dynamical analysis for the atomic displacement in the phase transition has not been reported yet. This thesis reports about the prediction of the new route of phase transition from β-Ti_3O_5 to λ-Ti_3O_5 under uniaxial tensile. Also, the mechanism for the phase transition is discussed, by a standpoint of theoretical calculation.

Phase transition under uniaxial tensile

To evaluate the atomic-scale dynamics of phase transition, molecular dynamics (MD) calculation was employed for this research. MD calculation can be classified into two types, classical one and *ab initio* one, of which deference is that their potential field is constructed of empirical or not. In this research, both types were applied. Classical MD was performed with LAMMPS package, and *ab initio* MD was performed with OpenMX package, respectively. Crystal structure of β-Ti_3O_5 was constructed from the reported values in a previous research [3]. In a classical MD simulation, a supercell with 8000 atoms (1000 chemical formulas of Ti_3O_5) was prepared. To decrease the computational cost, a primitive unit cell with 16 atoms (2 chemical formulas) was applied for *ab initio* MD. The largest difference between β and λ-Ti_3O_5 unit cell is *c*-axis. λ-Ti_3O_5 has 6 % longer *c*-axis than that of β-Ti_3O_5, implying that uniaxial strain or stress against *c*-axis will strongly contribute to the phase transition. Based on this idea, classical MD of β-Ti_3O_5 by gradually applying uniaxial stress on *c*-axis was performed. In the calculation, temperature was controlled at 300 K, by isothermal-isobaric (NPT) ensemble. Specific atomic displacements especially Ti(3) and O(5) sites began around 5 GPa of tensile stress (8000 calculational steps,) consequent to the structural phase transition from β-Ti_3O_5 to λ-Ti_3O_5. There is an assumption that Ti(3) and O(5) sites will largely move in the phase transition from the similarity of these two structures, though this dynamics is not confirmed by experimental nor theoretical way. The atomic displacement was not occurred simultaneously in all part of the supercell, but one-by-one site. Length of *c*-axis drastically increased up to 10 % compared to the initial β-Ti_3O_5 structure synchronized with the displace of Ti(3) and O(5). At 6.6 GPa (10000 steps,) whole cells completed phase transition to λ-Ti_3O_5 structure. In the case of isothermal-isovolumic (NVT)

calculation under uniaxial strain on *c*-axis of initial β-Ti_3O_5 structure, phase transition from β-Ti_3O_5 to λ-Ti_3O_5 was also observed at the tensile strain-induced unit cell. This phase transition was successfully observed in both classical and *ab initio* MD.

Phonon softening under uniaxial strain

Phonon softening is one of the well-known theories to discuss a mechanism of displacive structural phase transition [4]. In this theory, a frequency of the specific phonon vibration mode decreases (softening,) as the precursor phenomena to the phase transition, and its vibrational direction corresponds to the one of displacements in the phase transition. Displacement of Ti(3) and O(5) atoms occurs in the structural phase transition between β and λ-Ti_3O_5, and it is assumed to be a relationship with phonon softening. To discuss the mechanism of tensile-induced phase transition, dependence of phonon under *c*-axis uniaxial strain was calculated. The calculation was performed with OpenMX and ALAMODE code, by frozen phonon method. β-Ti_3O_5 structure with a supercell of 64 atoms (8 chemical formulas.) All of simulation cells were set as periodic boundary. As increasing lattice strain on *c*-axis, specific optical modes' frequency decreased, especially around Γ point. Also, in the case that tensile strain is applied against *c*-axis of β-Ti_3O_5, the atomic displacement direction in the vibrational modes at the minimum and the second from the minimum frequency corresponded as the one observed in the displacement phase transition. This suggests the relationship between phonon softening and strain-induced phase transition from the viewpoint of movement of atoms.

Conclusion

This research suggests the phase transition route from β-Ti_3O_5 to λ-Ti_3O_5, by tensile stress or strain, and analyzed its dynamics of an atomic displacement. Also, the mechanism of the phase transition was discussed by the relationship of phonon-softening and deformation on a unit cell. It is the first time to discover the tensile-induced phase transition by MD calculation for Ti_3O_5, and to succeed in obtaining atomic-scale dynamics in a phase transition between β and λ-Ti_3O_5. Observed dynamics of atomic displacement in the phase transition was corresponded to the one that has been assumed in the previous research, yet it has not been revealed. This newly found phase transition route suggests the realization of large size single crystalline λ-Ti_3O_5, still not realized as a non-dope system, by applying tensile force against a β-Ti_3O_5 single crystal.

References

[1] S. Ohkoshi, Y. Tsunobuchi, T. Matsuda, K. Hashimoto, A. Namai, F. Hakoe, H. Tokoro, Nat. Chem. **2**, 539 (2010).

[2] H. Tokoro, M. Yoshikiyo, K. Imoto, A. Namai, T. Nasu, K. Nakagawa, N. Ozaki, F. Hakoe, K. Tanaka, K. Chiba, R. Makiura, K. Prassides, S. Ohkoshi, Nat. Commun. **6**, 7037 (2015).

[3] S.Åsbrink and A. Magnéli, Acta Cryst. **12**, 575 (1959).

[4] W. Cochran, Phys. Rev. Lett. **3**, 412 (1959).

-Table of Contents-

Chapter 1 General Introduction 1

1.1 Phase transition phenomenon 1

1.1.1 Examples for phase transition 1

1.1.2 Classification of phase transition by its order 2

1.2 Phase transition phenomena in Pseudo-brookite-type Ti_3O_5 3

1.3 Methods for assuming or evaluating structural phase transitions 4

1.3.1 Evaluating method for the phase transition against strain 4

1.3.2 Molecular Dynamics 6

1.3.3 Improved Reaction Dynamics Analysis Method 11

1.3.4 Softening of phonon dispersion 13

1.4 Objectives of this study 14

Figures and tables for chapter 1 15

Chapter 2 Electronic structure calculations of β- and λ-phases of Ti_3O_5 20

2.1 Introduction for this chapter 20

2.2 Software for calculation 20

2.3 Evaluation of onsite Coulomb interaction 20

2.4 Evaluation of potential energy under lattice strain 21

2.5 Analysis of electronic states 22

2.6 Analysis of precursor phenomenon in phase transition by lattice dynamics 24

2.6.1 Calculational method 25

2.6.2 Softening of phonon mode in strain-induced β-Ti_3O_5 on *c*-axis 25

2.7 Conclusion for chapter 2 27

Figures and tables for chapter 2 28

Chapter 3 Calculation of the phase transition from β-phase to λ-phase by molecular dynamics 54

3.1 Introduction for this chapter 54

3.2 Simulation of phase transition by ab-initio molecular dynamics 54

3.2.1 Observation of phase transition from β-phase to λ-phase 54

3.2.2 Analysis of the AIMD result 55

3.3 Classical molecular dynamics 56

3.3.1 Calculational method 56

3.3.2 Construction of a model for calculation 57

3.3.3 Structural relaxation of β-phase Ti_3O_5 58

3.3.4 NVT ensemble under fixed strain 59

3.3.5 Calculation under continuously stress-inducing condition 59

3.3.6 Phase transition from β-phase to λ-phase by increasing temperature 62

3.4 Conclusion for this chapter 63

Figures and tables for chapter 3 65

Chapter 4 Conclusion for the research 99

Acknowledgements 101

References 102

List of the paper related to the thesis 106

Chapter 1　General Introduction

1.1 Phase transition phenomenon

As an example, liquid water at room temperature becomes solid ice when cooled, and boils into water vapor when heated. The phenomenon of a material changing its macroscopic state due to a change in the external environment is called a phase transition, and each state classified by a phase transition is called a phase, which has been widely studied. Since the research on phase transitions is very diverse, in this section we will review the phase transitions between solid phases in solid-state physics and chemistry.

1.1.1 Examples for phase transition

・Magnetic Phase transition[1]

Electrons have spins, and when a magnetic field is applied to a material, magnetization occurs when the spins in the material are aligned parallel to the magnetic field. When a magnetic field is applied to a material, magnetization occurs when the spins in the material are aligned parallel to the magnetic field. The property in which the spins are aligned identically to the magnetic field and are maintained even when the magnetic field is removed is called ferromagnetism, while the state in which the spins are antiparallel and do not exhibit magnetism is called antiferromagnetism. The phase transition phenomenon in which ferromagnetism or antiferromagnetism is ordered by an external field such as a certain temperature or pressure is called a magnetic phase transition. Both typical ferromagnetism and antiferromagnetism become paramagnetic above a certain temperature, and the temperatures at which they change to paramagnetism are called the Curie temperature and the Neel temperature, respectively.

・Ferroelectric phase transition

If we qualitatively classify the current response when an electric field is applied to a material, the material through which the current flows is called a conductor, and the material through which the current does not flow or is very difficult to flow is called an insulator or semiconductor. At this time, insulators exhibit dielectric properties in which no flow occurs in the electrons inside the material, but instead electrical polarization occurs. Among these, there are some materials that under certain environmental conditions such as temperature and pressure, spontaneous polarization occurs inside the material. When an electric field in the opposite direction of the polarization is applied to this material, the polarization reverses in the direction of the electric field, which is called ferroelectric material. This property was discovered in the first half of the 20th century in Rochelle salt [2] and barium titanate [3], and today it plays a very important role not only in basic scientific properties but also in industrial applications such as piezoelectric devices and actuators.

・Structural phase transition.

A phase transition in which the structure of atoms inside a solid change under certain external environmental conditions is called a structural phase transition. Here, structure refers to changes in the lattice constant, symmetry, and microscopic atomic coordination structure of the crystal lattice. For this reason, ferromagnetic and superconducting phase transitions that do not involve atomic displacements do not correspond to structural phase transitions. Structural phase transitions can be classified into displacive transition and order-disorder transition.

・Displacive phase transition.

Phase transitions in which specific atoms in the crystal are uniformly displaced are called displacement-type phase transitions. As an example, $BaTiO_3$, which has a perovskite-type structure, has a cubic crystal at high temperatures, a tetragonal crystal below 130 °C, and orthorhombic and trigonal crystals at lower temperatures [3]. During the structural phase transition from cubic to tetragonal, the symmetry is reduced due to the elongation of the lattice length in one axis, and the Ti atoms located in the center of the unit lattice are slightly displaced in the *c*-axis direction, causing polarization in the lattice and the development of ferroelectricity.

・Order-disorder phase transition.

This is a phase transition in which the atoms and molecules in the crystal are oriented in the same direction and become ordered below a certain temperature Tc, but above Tc, the orientation is reduced or eliminated, resulting in a disordered state; examples include NH_4Cl [4] and the $L1_0$-type-face-centered cubic (fcc) phase transition in binary alloys [5].

1.1.2 Classification of phase transition by its order

In this section, we will discuss the relationship between Ehrenfest's classification of phase transitions and Landau's potential polynomial for states. Ehrenfest determined that n^{th} order phase transition has discontinuous n^{th} order derivative by external variables, which determine the system’s environment, such as temperature or pressure against Gibbs free energy in the system [6]. The first-order phase transition is a discontinuity in the entropy, which is the first-order partial derivative of the Gibbs energy due to temperature, or in the volume obtained by the first-order partial derivative due to pressure. At this time, the Gibbs energies of the two phases before and after the phase transition intersect at a single point, and the two phases coexist at this intersection point. In the second-order phase transition, the Gibbs energy changes continuously before and after the phase transition, and the coexistence of the two phases is not observed.

On the other hand, in Landau's phenomenology of phase transitions, the free energy is expressed as a polynomial in terms of the order variable p that characterizes the system [7]. Since the coefficients in these polynomials are functions of the external field variable a, the curvature of the free energy curve changes with the change in a, and the phase transition point can be expressed. The second-order phase transition can be expressed as a fourth-order equation, and at the phase transition point $a = a_0$, the curve becomes monotonically negative between the start and end states, and the phase transition occurs to the end state where the free energy is relatively stable. The monotonicity of the curve indicates that the phase transition is spontaneous (Fig. 1.1(a)). On the other hand, the first-order phase transition requires the free energy to be expressed as a sixth-order polynomial or higher. This is because the first-order phase transition occurs when the free energies of the start and end states are equal, and the existence of a metastable state is required, but the fourth-order function can only represent the spontaneous phase transition and cannot represent the metastable state, which is a state with local minimum energy. However, fourth-order functions can only represent spontaneous phase transitions, and cannot represent metastable states, which are states with local minimum energy. By expressing the free energy in a sixth-order equation or higher, it is possible to represent the starting state of a metastable state because there is an energy maximum, or barrier, between the two states even at the phase transition point where the Gibbs energies of the starting and final states are equal (Figure 1.1(b)).

1.2 Phase transition phenomena in Pseudo-brookite-type Ti_3O_5

Tri-titanium pentoxide Ti_3O_5 has several crystal structures (phases) with the same composition, and five phases, α, β, γ, δ, and λ, have been reported so far [8-10]. These five phases can be classified into two major structural groups: α, β, and λ belong to the analogous Pseudo-Brookite or Anosovite type, and γ and δ belong to the Magneli type (Figure 1.2). In this study, we focus on the former.

The structure of pseudo-Brookite was reported in 1930 as the composition of Fe_2TiO_5 [11], and many solid solutions of titanium oxides and other metal oxides with a similar structure have been reported, including armalcolite found in moonstone [12]. These are represented by the generalized chemical formula $M_xTi_{3-x}O_5$ ($0<x\leqq2$) with titanium, oxygen, and other metal elements M. Many substitution systems have been reported for the metal element M, including Fe [11,13], Al [14,15], Sc [16,17], Mg [18-21], Ga [22], Co [23,24], and a few nitrogen-substituted $Ti_{3-\delta}O_4N$ anions have been reported [25]. If M=Ti, it corresponds to the Pseudo-Brookite-type Ti_3O_5 described above.

The α-phase structure with Cmcm symmetry is found only above 500 K in pure Ti_3O_5 and is stabilized at room temperature by partial substitution of Ti sites by metallic elements [15,18,21]. β-phase is obtained by cooling α-phase below 450 K. λ-phase is a monoclinic structure with C2/m symmetry like β-phase, but the atomic coordination structure in the crystal lattice is different from that of β-phase and is slightly distorted from α-phase. In the temperature range between those of β and α (450 K~500 K), a high-temperature monoclinic (HM) phase with a structure similar to that of λ-phase exists [26], but its detailed physical properties have not been clarified.

λ-phase was isolated as nanoparticles at room temperature in 2010, and a structural phase transition to β-phase was found under light irradiation [8] and pressure [27,28]. From specific heat measurements, the phase transition in this case is considered to be first-order. Isolation of λ-phase Ti_3O_5 in the metastable state has been obtained only in nanoparticles [8,29,30] and thin films [31,32], where size effects contribute, and no bulk-sized single crystals have been obtained at room temperature and atmospheric pressure, except for stabilization by doping with metallic elements [33].

The first major difference between both λ-phase and β-phase structures is the lattice constant. As shown in Table 1.1, the *c*-axis of β-phase is contracted by about 6 % compared to that of λ-phase, and the *a*- and *b*-axes also differ by about 1 %. The second difference is the displacement of the Ti(3) site and the change in the oxygen coordination structure around it, as shown in Figure 1.3. In both phases, the unit lattice contains 8 inequivalent atomic sites. The conventional cell shown in Figure 1.3 contains four atoms at each site. Focusing on the neighboring oxygen atoms around Ti(3), λ -phase has three O(3) sites, one O(2) site, and two O(5) sites, while in β-phase, the number of O(3) sites is reduced to two in the *b*-axis direction, and instead, O(4) sites are in close proximity. This difference in structure can be interpreted as the rotational displacement in the ac plane of Ti(3), O(5), and O(3) coordinated in the *b*-axis direction relative to Ti(3). Therefore, the phase transition between the β and λ-phases is expected to be an atomic displacement type phase transition with changes in the lattice parameter and coordination structure. However, atomic-scale dynamics in this phase transition is not observed experimentally nor predicted by theoretical calculation, only analogously assumed by the similarity of their crystal structure. In 2021, propagation of phase transition in a photo-induced phase transition from β to λ-phase by analyzing its change of lattice constants with high-time resolution diffraction pattern as 500 fs [34], but the phenomena related to the atomic displacement motion itself, such as thermal diffuse scattering of specific diffraction peaks, were not observed. The atomic displacement associated with the phase transition is thought to occur and be completed on a shorter scale.

1.3 Methods for assuming or evaluating structural phase transitions

As described in section 1.2, phase transition phenomena observed in Pseudo-Brookite type Ti_3O_5 can be assumed to be a displacive structural phase transition with the change of lattice their constants and coordination structure of atoms in their unit cell. This section shows the theoretical way to analyze such displacive structural phase transition, mainly adopted in this research.

1.3.1 Evaluating method for the phase transition against strain

Consider a situation in which a crystal lattice is deformed by extension or compression and reaches an equilibrium state. At this time, the crystal lattice is given work by the external force that causes deformation (strain), and the internal energy is increased. In addition, stress is generated from inside the crystal lattice to balance the external force.

One way to evaluate the static energy against lattice strain in solid crystals is to assume that the energy change against strain is elastic. To the extent that the lattice responds elastically to strain, the energy change due to strain can be fitted as a quadratic harmonic function of the amount of strain. If we consider the amount of energy change ΔU required to apply a small strain Δl to the lattice, the ratio $\Delta U/\Delta l$, *i.e.*, the slope of the tangent line in the energy-strain curve, corresponds to the force required to apply the strain from the outside. By dividing this by the cross-sectional area of the surface where the force is applied, the stress on that surface can be obtained. When two phases with different structures are compared on the basis of a common criterion such as lattice length or volume, the lattice constant that gives the minimum value of the internal energy and the minimum value of the lattice constant are different, and the phase stability of each structure can be determined. The (static) free energy of a system at a finite temperature T and a finite pressure P can be written as equation (1.1), taking into account not only the cohesive energy but also the external work due to pressure and the contribution of the entropy term.

$$\Delta G = U + P\Delta V - T\Delta S \qquad (1.1)$$

In equation (1.1), ΔV is the volume change from zero pressure to equilibrium state, and ΔS is the entropy change from zero temperature to temperature T.

When two phases A and B undergo a phase transition at temperature T and pressure P, the relationship between the free energies of the two phases, $\Delta G_A = \Delta G_B$, is established. In the case of solids, since ΔS can be regarded as a very small value compared to U and $P\Delta V$, it is possible to estimate the possibility of phase transition by ignoring the contribution of this term from Equation (1.1) and comparing the enthalpies of the two phases, $\Delta H = U + P\Delta V$. That is, when the enthalpies of the two phases are equal, an inter-solid phase transition may be induced, although the activation barrier needs to be taken into account.

We now consider the case where a common tangent is given between the two energy curves in the two different phases, A and B. Here, for simplicity, we consider the strain to be isotropic and the energy change to be a function of volume change. A derivative coefficient of energy-volume function has a dimension of energy/volume, thus, pressure. By multiplying area to pressure, we can obtain the force required to apply small deformation against the system. If a common tangent line with slope p_0 can be drawn between the two phases, and the volume difference giving the tangent line is $V_A - V_B = \Delta V$, then the energies E_A and E_B of phases A and B are related by the relation (1.2).

$$E_A(V=V_A)=E_B(V=V_B)+p_0\Delta V \qquad (1.2)$$

This means that phase A and phase B are in a state of equal enthalpy at stress p_0, suggesting the existence of a stress-induced phase transition, although the existence of an activation energy barrier is unknown. For example, if $V_A<V_B$ and $E_A(V=V_A)>E_B(V=V_B)$, $p_0<0$, which corresponds to the transition from the low-pressure phase B to the high-pressure phase A due to the pressure-induced phase transition. Conversely, if $V_A>V_B$ or $E_A(V=V_A)>E_B(V=V_B)$, then $p_0>0$ and $\Delta V>0$, which means a phase transition from B (relative high-pressure phase) to A (low-pressure phase) due to volume expansion. By applying this method, the experimentally unexplained high-pressure phase structure has been predicted [35].

1.3.2 Molecular Dynamics

Molecular Dynamics (MD) is a theoretical calculation method in which particles such as atoms are subjected to motion based on the classical Newtonian equations of motion, and their time evolution is analyzed by computer.

Historically, it was first applied to a hypothetical rigid sphere [36], and then to argon liquid [37]. Molecular dynamics has provided very useful knowledge in materials science, not only for reproducing experiments such as the analysis of phase transition mechanisms, but also for making theoretical predictions for systems that are difficult to realize by experiments, such as the prediction of high-pressure phase transitions. The basic calculation procedure of molecular dynamics method is as follows:

(1) Calculate the potential energy and force due to the interaction, kinetic energy, and other thermodynamic parameters such as temperature and pressure of the system for the arrangement of the atomic population to be calculated at a certain time t.

(2) Update the spatial coordinates and velocities of the atoms by giving the group of atoms a motion that follows Newtonian mechanics from the velocity and force, and advancing the time by Δt from t.

(3) Repeat the above steps (1) and (2) to obtain the trajectories or statistical properties of the atoms over a long time.

The motion of an atom is most simply obtained by calculating the Newton equation of motion from the potential energy $U(\{r_i\})$ of the system, which is a function of the nuclear coordinates, and the kinetic energy in the equation below;

$$K=\frac{1}{2}\sum_{i=1}^{3N} m_i v_i^2$$

In molecular dynamics, the equation of motion is treated as a differential equation, and the overall trajectory is obtained by solving the position and velocity differentially at each time and integrating them numerically. The Verlet method is described as one of the representative calculation methods [38].

A force against a specific atom and direction of *N* atoms in three-dimensional space, F_i ($1<i<3N$), can be written as formula (1.3);

$$F_i = m_i a_i = \frac{m_i dv_i}{dt} \qquad (1.3)$$

In formula (1.3), a_i is acceleration of an atom.

If the system is in an equivalent state, there is a relation between potential *U* and F_i written as formula (1.4).

$$F_i = -\frac{dU}{dr_i} \qquad (1.4)$$

Also, specific atom's velocity vi can be represented as formula (1.5).

$$v_i = \frac{dr_i}{dt} \qquad (1.5)$$

From the equality of Fi in formula (1.3) and (1.4), we can obtain formula (1.6), hence, 6*N* simultaneous equation can be obtained from (1.5) and (1.6).

$$v_i = \frac{dr_i}{dt}$$

$$\frac{dv_i}{dt} = \frac{1}{m_i}\frac{\partial U}{\partial r_i} \qquad (1.6)$$

In the formulas, atomic mass mi and potential *U* is already known and given as a premise, we can calculate F_i and a_i. Next, we will represent the time-revolution of atomic position r_i by applying these already-known or computable values.

By applying amount for a time-revolution Δt small enough, position ri in an advanced time can be represented by Taylor expansion of Δt. Also, formula (1.7) can be obtained by truncate higher-term than third coefficient.

$$r_i(t + \mathit{\Delta} t) = r_i(t) + v_i(t)\mathit{\Delta} t + \frac{1}{2}a_i(t)\mathit{\Delta} t^2 \qquad (1.7)$$

Then, by applying finite difference method, we will remove unknown value v_i.

The "past" position, $r_i(t\text{-}\Delta t)$, can be obtained just substitute minus Δt onto formula (1.7);

$$r_i(t - \mathit{\Delta} t) = r_i(t) - v_i(t)\mathit{\Delta} t + \frac{1}{2}a_i(t)\Delta t^2$$

$v_i(t)$ can be removed by sum up these two formulas. Also, by substituting (1.3), we can calculate the position at the time of $t+\Delta t$ from the position at the time of *t* and $t\text{-}\Delta t$.

$$r_i(t + \Delta t) \cong 2r_i(t) - r_i(t - \Delta t) + \frac{F_i(t)}{m_i}\Delta t^2 \qquad (1.8)$$

However, this "simple Verlet method" has large numerical error. To improve accuracy, "velocity Verlet method", which use velocity formula shown in below, with more shorter amount of time-revolution

[39].

$$v_i(t+\frac{\Delta t}{2}) = v_i(t) + \frac{F_i(t)}{2m_i}\Delta t$$

When performing molecular dynamics calculations, atomic populations are required to follow some statistical thermodynamic state of the system, i.e., an ensemble. Typical ensembles include small canonical populations where the number of particles, energy, and volume of the system are constant (microcanonical ensemble, adiabatic system) and canonical populations where the number of particles, temperature, and volume are constant (canonical ensemble, isothermal heat bath system). The parameters to be kept constant are the number of particles *N*, internal energy *E*, volume *V*, temperature *T*, and pressure or stress *P*. Depending on the combination of parameters to be controlled, the corresponding alphabet is used, for example, NVE (isovolumic and constant energy, small canonical), NVT (isovolumic and isothermal, canonical), NPT (isothermal and isobaric or isostatic stress). These thermodynamic parameters are given in the calculation of procedure (1) above, and any differences from the specified values are corrected and controlled to avoid large deviations from the target values.

First, the temperature is calculated from the kinetic energy of the atomic population. In statistical thermodynamics, the velocity of a group of atoms at a given temperature *T* follows a Maxwell-Boltzmann distribution, and the sum of their kinetic energy can be written as a formula below, where k_B is Boltzmann's constant;

$$\left(\frac{1}{3N}\right)\sum mv^2 = \frac{k_B T}{2}$$

Here, the motion is independent of each component in 3-dimensional space, and the number of atoms is *N*. Using this property, molecular dynamics calculates the measured temperature of the system at a given time, T_{MD}, by back-calculating the total kinetic energy of the atomic population, shown above.

$$T_{MD} = \left(\frac{2}{3Nk_B}\right)\sum mv^2$$

When temperature is not included in the control conditions of an ensemble, such as NVE, for example, the temperature of the system is only measured, and in the equilibrium state, it fluctuates slightly from time to time.

On the other hand, if temperature is included as a control condition, the temperature of the system needs to be corrected at each time and calculation step. There are two typical correction methods: the velocity scaling method and the Nose'-Hoover method.

The velocity scaling method adjusts the calculated velocity at each time step so that the average value matches the target temperature at the next step, while the Nose'-Hoover method incorporates the contribution of the heat bath that contacts the atomic population in the NVT ensemble to control the temperature into the equation of motion of the system [40-42]. First, the Lagrangian from which the equation of motion of the microcanonical ensemble system is derived can be written as below;

$$L = K - U = \frac{1}{2}\sum_{i=1}^{3N} m_i v_i^2 - U$$

Based on this, the extended Lagrangian was given by Nose', with the contribution of the heat bath to keep the temperature constant;

$$L = \frac{1}{2}\left[\sum_{i=1}^{3N} m_i s^2 v_i^2 - U\right] + \frac{Q}{2}\left(\frac{ds}{dt}\right) - g k_B T \ln s$$

Corrections are added to the equations of motion derived from this Lagrangian to obtain a series of equations of motion (1.9).

$$v_i = \frac{dr_i}{dt} \qquad (1.9.1)$$

$$\frac{dv_i}{dt} = -\frac{1}{m_i}\frac{\partial U}{\partial r_i} - \frac{d\xi}{dt} v_i \qquad (1.9.2)$$

$$\xi = \frac{d\ln s}{dt} \qquad (1.9.3)$$

$$\frac{d\xi}{dt} = \frac{1}{Q}\left[\sum_{i=1}^{3N} m_i v_i^2 - 3Nk_B T\right] \qquad (1.9.4)$$

In this, the parameter ξ represents the difference between the kinetic energy of the system and the target kinetic energy obtained from the target temperature. This term, given in the second term on the right-hand side of equation (1.9.2), acts as a virtual frictional force on the time evolution of velocity v_i, and can be used to correct velocity v_i so that it does not deviate significantly from the target temperature. It can be seen that Q in the denominator of equation (1.9.3) is a term that determines the weight of the correction to v_i by ξ. In the actual calculation, it is a parameter that is corrected to the optimum value after checking the difference between the temperature obtained from the output and the target temperature.

Next, we discuss the Parrinello-Rahman method [43], which is a typical method for stress control of systems. In the NVT ensemble, only the equations of motion of the molecules are considered, but in the NPT ensemble, the equations of motion of the wall pistons are also taken into account. In the NVT ensemble, only the equations of motion of the molecules are considered. Just as a heat bath (thermostat) is required as a computational controller to keep the temperature constant, a controller is required to control the pressure or stress, which is called a barostat. This control enables volume-variable molecular dynamics calculations, and is suitable for molecular dynamics calculations of, for example, pressure-induced phase transitions in which not only the atomic configuration but also the crystal lattice size changes simultaneously under equal pressure.

One of the most important conditions for molecular dynamics calculations is the determination of the potential and force of the system. Since this determination method is subdivided into several parts, we will discuss each calculation method in the following.

・Classical Molecular Dynamics

In the classical method, the potential is obtained by a (semi-)empirical formula. The formulae range from simple distance functions, such as the Morse and Lennard-Jones potentials, to those with charge effects, such as the Beest-Kramer-Santen (BKS) potential, to the ReaxFF potential, which integrates them. While these potentials have the advantage of low computational time (cost) and the ability to handle a large number of atoms, they have the disadvantage of limited applicability because they require the creation of potentials for individual target systems, such as combinations of element types, coordination structures, and bond distances.

・Ab initio Molecular Dynamics (AIMD)

AIMD is a method to calculate molecular dynamics from first-principles potentials in order to overcome the limitation of applicable systems due to potential dependence, which is a major problem in classical molecular dynamics. The wavefunction for the atomic configuration at a certain time is given from the wavefunction calculated self-consistently by the usual first-principles procedure, and the procedure of calculating the force, updating the coordinates, and calculating the wavefunction again follows the general molecular dynamics method. However, the number of atoms that can be calculated is small and the calculation time is long because the calculation cost of the first-principles calculation itself is very high.

・Car-Parrinello Molecular Dynamics (CPMD) [44]

AIMD is a serial calculation in which the wavefunction and the atomic positions are updated alternately at each step. On the other hand, Car and Parrinello proposed a different method from AIMD in 1985, called Car-Parrinello Molecular Dynamics (CPMD), in which the equations of motion of the nuclei as well as the equations of motion of the wavefunctions are hypothetically set up, and the time evolution of each is obtained independently. In this way, the update of the nuclear coordinates and the wave function are processed in parallel, which reduces the computation time. However, this method requires a sufficiently small amount of time evolution per calculation step to prevent the divergence between the nuclear coordinates and the wave function, and is difficult to apply to systems where the nature of the wave function changes significantly.

・Machine learning molecular dynamics method [45]

This is a computational method proposed in the late 2010s that combines machine learning. First, the target large-scale system is subdivided into smaller systems, and the energies and interactions in each subdivision are obtained, which are then added together to obtain the overall properties. Based on the assumption that the subdivided system belongs to a certain statistical thermodynamic ensemble, a large number of teacher data are created by Monte Carlo method, and the time evolution of the thermodynamic properties of the unknown system is obtained based on the database of coordinate configurations and energies calculated by first-principles calculation in advance. This method has the advantages of both CMD and AIMD in terms of computational speed and scale of applicability, although it requires the cost of constructing the teacher data in advance.

Finally, some examples of applications of molecular dynamics are described here. Although molecular dynamics can be applied to many phenomena related to the motion of matter, it can be broadly classified into two purposes.

The first is the application to dynamic evaluation of the time evolution of a system. In molecular dynamics calculations, it is possible to not only follow a certain thermodynamic ensemble, but also to stochastically exceed the activation energy barrier to other states by appropriate settings, for example, by increasing the temperature. This makes it possible to simulate, for example, the freezing point of molecules [48], adsorption phenomena on metal surfaces [49], diffusion phenomena [50], structural changes in large molecules such as polymers and proteins [51], and structural phase transitions induced by external fields such as temperature, pressure, and light [52-56].

The second application is the sampling of states to obtain statistical thermodynamic properties. Based on the ergodic property, by controlling the molecular dynamics calculations to a given thermodynamic ensemble in a sufficiently large number of steps, the states of a series of computational systems can be mapped to the states in the phase space specified by the ensemble at an equal weighting rate. By taking advantage of this property, molecular dynamics calculations can be performed without extreme structural changes such as structural phase transitions, and by sampling multiple structures from the set of structures obtained in the time evolution and statistically analyzing information such as coordinates and lattice constants, it is possible to obtain the phonon frequencies [44], thermal expansion coefficients at finite temperatures [57]. This method provides information that corresponds to random sampling in the Monte Carlo method. In recent years, it has been applied to the extraction of supervisory data for constructing machine learning potentials [58], and to sampling for calculating phonons with anharmonic terms at finite temperatures [59].

1.3.3 Improved Reaction Dynamics Analysis Method

As mentioned in the previous section, molecular dynamics calculations are very useful as a computational method to obtain dynamic and statistical information related to materials. However, due to its computational cost, there are significant time and space limitations on the systems to which it can be applied. In other words, the larger the number of atoms to be calculated and the longer the number of simulation steps (the time evolution of the system represented by the calculation), the higher the calculation cost. In particular, the time evolution must be calculated in series, and the amount of time evolution per step must be about 1 femtosecond (1 fs=10^{-15} sec.), so the maximum number of steps that can be calculated in reality is about 10^6 steps, or nanoseconds (=10^{-9} sec.). On the other hand, in realistic experimental systems, a series of reactions or changes may take more than a nanosecond, or even a microsecond or millisecond. According to the transition state theory [60,61], the reaction frequency ν at a certain temperature T(K) can be expressed as Equation (1.10);

$$\nu = \frac{k_B T}{h} \exp\left(-\frac{\Delta E}{k_B T}\right) \quad (1.10)$$

where ΔE is the height of the transition energy barrier located at the reaction coordinate from the starting state to the final state, k_B is Boltzmann's constant, and h is Planck's constant. If we assume ΔE=1 eV and T=500 K, the reaction rate is ν=2 sec.$^{-1}$, that is, once every 0.5 second. To observe this phenomenon by molecular dynamics would require more than 0.5 second, or 5×10^{14} steps if we assume 1 fs/step, which is practically impossible to calculate. Thus, molecular dynamics is particularly difficult to apply to the analysis of reactions with high activation barriers in terms of the number of calculation steps. In this section, we will introduce a method to overcome this problem.

・Nudged Elastic Band (NEB) method [62]

The NEB method is a type of structural optimization with limiting conditions based on the assumption that the starting and ending states of the reaction are fixed and the reaction proceeds via the minimum energy barrier existing between them. First, based on the expected reaction pathway, the structure of the reaction in progress is artificially set. This is done, for example, by interpolating the transition of the atomic coordinates between the start and end states into multiple stages, and preparing a set of structures in which the displacement proceeds step by step. By energy-optimizing these structures, we can estimate the energy barrier between the start and end states. At this time, a penalty (virtual energy barrier between structures and states) is given between each structure to prevent over-optimization and transition to another structure. This method makes it possible to calculate thermally excited phenomena such as atomic diffusion [63] and dislocation formation inside metals [64]. The NEB method has also been reported to estimate the activation barrier in the β- and λ-phase Ti_3O_5, the material of interest in this study [65].

・Molecular dynamics calculations with restrictions

In molecular dynamics calculations, restrictions are placed not only on the ensemble conditions of the system, but also on parameters such as energy and reaction coordinates to force the system to overcome the energy barrier.

Examples of such methods include the metadynamics method, in which the reaction is accelerated by filling in the valleys of the potential minima of the starting states with artificial potentials [66], and the Blue-Moon ensemble method, in which low-probability states are sampled preferentially [67].

1.3.4 Softening of phonon dispersion

This theory was proposed to interpret the phenomenology in ferroelectric phase transitions with displacements [68,69], and the structural phase transition can be considered from the potential curve and phonons by Landau. The crystal lattice is vibrating at a very small rate even in the equilibrium state, and a simple model can be considered in which the atoms are connected as harmonic oscillators (Figure 1.4) [70]. In this case, if a small displacement Δr is given to one atom, the potential change $\Delta\varphi$ can be written as follows, using a constant k;

$$\Delta\phi = k\Delta r^2$$

In harmonic oscillation, the frequency ω can be expressed using k and the mass m of the atom as follows;

$$\omega = \sqrt{\frac{k}{m}}$$

On the other hand, as described in section 1.1.2, the free energy of a state in a phase transition can be expressed as a polynomial of the order variable p (displacement, polarization, etc.) with coefficients that are functions of the external variables a (temperature, pressure, etc.). If the starting and ending states are separated by a potential barrier, it can be approximated as a quadratic function near the equilibrium position between them. This corresponds to the elastic behavior of the entire system, and the harmonic lattice vibration is considered to be oscillating near the equilibrium position. In this case, the coefficient k corresponds to the sign of curvature of the quadratic function.

Looking at the curvature of the free energy curve at $a=a_0$, which gives the second-order phase transition, the curvature around the starting state is less than zero. This means that the coefficient k of oscillation of the system decreases to less than zero. Furthermore, the value of the frequency ω also decreases at this time, and since it is proportional to the square root of k, when k becomes negative, ω becomes imaginary. Thus, as we approach the phase transition point and the starting state becomes energetically unstable, the lattice frequency also decreases, and finally, when the coefficient of vibration becomes negative, we can see that a spontaneous phase transition occurs. As the coefficient of vibration, or spring constant, weakens, the spring becomes softer, capable of providing a large displacement with a small amount of force, and this decrease in the coefficient and frequency is called softening of the lattice vibration (or phonon). In the state of spontaneous phase transition, the spring coefficient is negative, *i.e.*, the more it is displaced, the more energetically stable it becomes, and the frequency becomes imaginary, which is called imaginary phonon. On the other hand, in the case of a first-order phase transition, the curvature of the local free energy remains positive because a potential barrier remains between the starting and ending states even at the phase transition point. However, as shown in Figure 1.4(b), the curvature decreases. Therefore, even in the first-order phase transition, softening can be observed as a precursor phenomenon of the phase transition.

In a three-dimensional *N*-atom lattice, first-order independent lattice vibrations can be obtained in 3*N* modes, of which 3 modes are acoustic modes and the remaining (3*N*-3) modes are optical modes. In the case of a displacive structural phase transition, the phase transition proceeds from the start state to the end state by displacing some atoms in the lattice. At the phase transition point, the energy of the atoms in the direction of displacement decreases, and the atoms become easier to displace. Therefore, soft phonons are generated in the vibration mode including this displacement direction, especially in the optical mode, which is a non-translational vibration when only certain atoms are displaced. When softening occurs in the acoustic mode, a ferroelastic phase transition related to the strain of the entire lattice without atomic displacement is induced.

As described above, it is possible to study the mechanism of displacive structural phase transitions by varying external variables such as temperature and pressure, and determining the change in phonon frequencies by experimental methods including Raman spectroscopy [71] and theoretical calculations. As an example of application, this method succeeded in explain the mechanism of ferroelectric phase transition with lattice deformation and displacement in $BaTiO_3$ [72], or structural phase transition in zirconium [73].

1.4 Objectives of this study

As mentioned in section 1.2, the dynamics of the phase transition between β-phase and λ-phase Ti_3O_5 is not yet understood. The global objective of this study is to theoretically clarify this phase transition dynamics. The specific goals of this study are, first, to investigate a method to evaluate the microscopic dynamics and mechanism of the displacement-type phase transition by theoretical calculations, and second, to search for a new phase transition route using this method.

This thesis is composed from four chapters. In chapter 1, this chapter, a standpoint and calculational techniques treated in this thesis is generally described. In chapter 2, structural, electrical and vibrational properties of Ti_3O_5 lattice was discussed with first-principle calculation. From the result, the possibility of the phase transition from β- to λ-phase by uniaxial tensile is suggested. In chapter 3, the dynamics of the phase transition was analyzed and discussed by molecular dynamics calculation. It makes clearly visualizes the dynamics and time-revolution of phase transition. Finally, chapter 4 concludes this research.

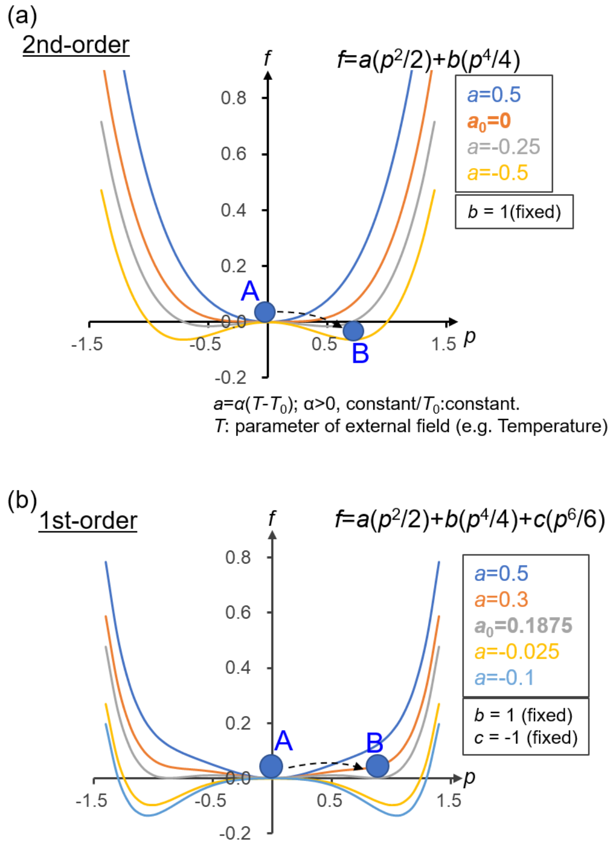

Figure 1.1 Representation of phase transitions with Landau free energy *f*, showing (a) second-order phase transition, and (b) first-order phase transition (lower panel). The curvature of *f*, which is a polynomial function of the order parameter *p* that characterizes the system, varies with the external variables *a*, *b*, and *c*. In the figures, *b* and *c* were set as $b = 1$ and $c = -1$ for simplicity. The second-order phase transition is represented as a fourth-order function of *p*, and the first-order phase transition is represented as a sixth-order function.

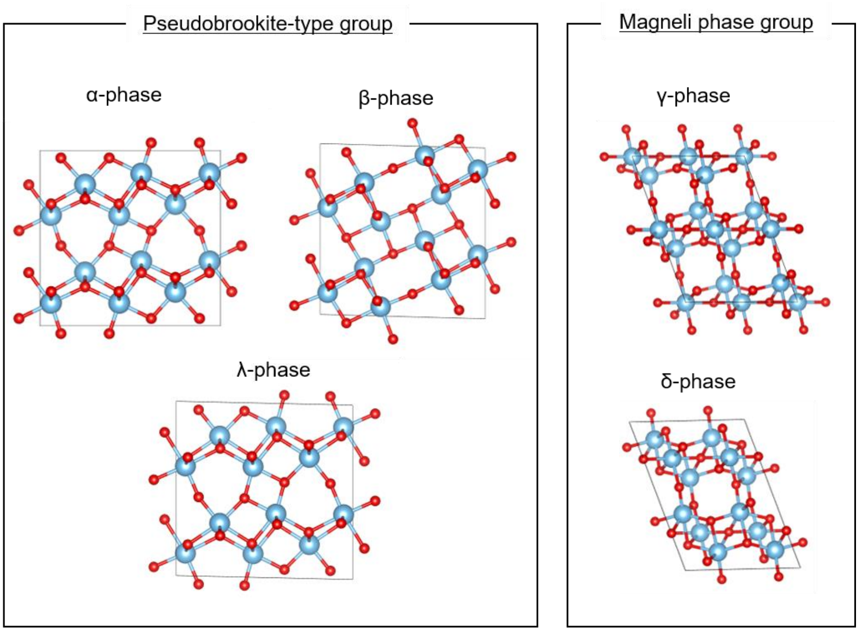
Pseudobrookite-type group
α-phase
β-phase
λ-phase
Magneli phase group
γ-phase
δ-phase

Figure 1.2 Five phases of tri-titanium pentoxide Ti_3O_5 and their classification by crystal structure. The figures were drawn by VESTA [74].

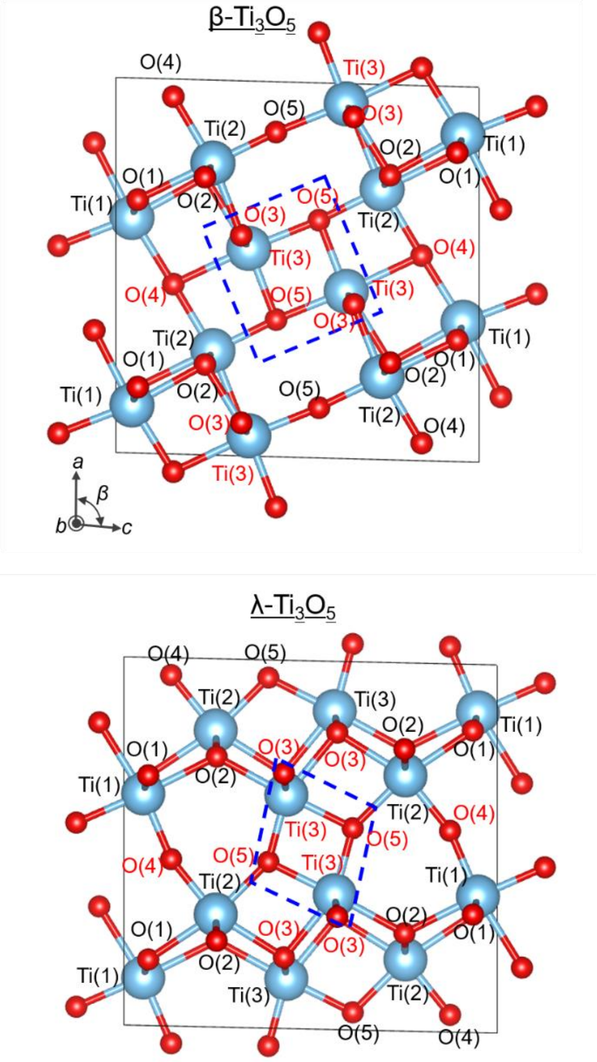
β-Ti3O5
O(4)
Ti(3)
O(5)
O(3)
Ti(2)
O(2)
Ti(1)
O(1)
O(1)
O(2)
Ti(1)
O(3)
O(5)
Ti(2)
Ti(3)
O(4)
O(4)
O(5)
Ti(3)
O(3)
Ti(1)
Ti(2)
O(1)
O(1)
O(2)
Ti(1)
O(2)
O(5)
Ti(2)
O(4)
O(3)
Ti(3)
a
β
b
c
λ-Ti3O5
O(4)
O(5)
Ti(2)
Ti(3)
O(2)
Ti(1)
O(1)
O(3)
O(3)
O(1)
Ti(1)
O(2)
Ti(2)
O(4)
Ti(3)
O(5)
O(5)
Ti(3)
O(4)
Ti(2)
Ti(1)
O(1)
O(3)
O(3)
O(2)
O(1)
O(2)
Ti(1)
Ti(3)
Ti(2)
O(5)
O(4)

Figure 1.3 Unit cell lattice of β-phase and λ-phase of Ti_3O_5. Both structures are shown with the *b*-axis in the Conventional Cell oriented perpendicular to the paper plane and the ac plane projected. Each structure and eight inequivalent sites (Ti(1)~(3), O(1)~(5)) are also shown. The Ti(3) and O(5) sites, which are significantly displaced in the phase transition between the two phases, and the O(3) and O(4) sites, whose coordination structure changes accordingly, are shown in red. The displacive structural transition between the two phases is interpreted to be caused by the in-plane rotation of the four-membered ring consisting of Ti(3) and O(5) sites, which are surrounded by blue dashed lines in the figure. The figure is drawn by VESTA [74].

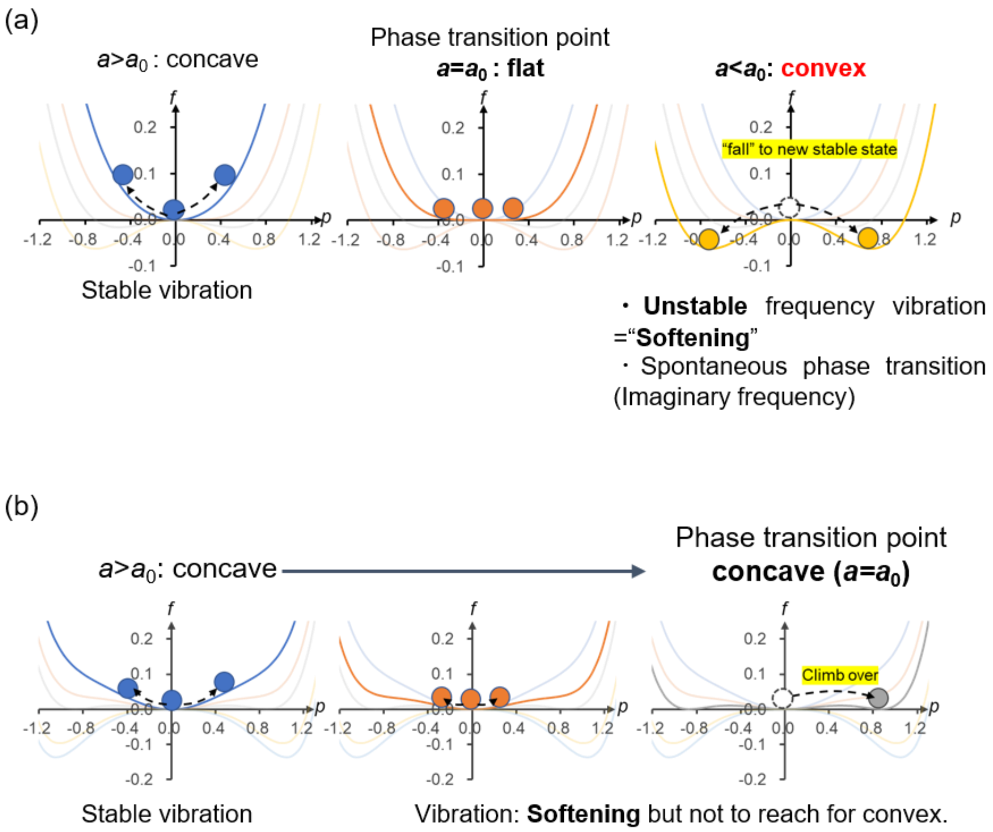

Figure 1.4 Relationship between the curvature of the Landau free energy *f* and the softening of the lattice vibration in the starting state, (a) the second-order phase transition and (b) the first-order phase transition. The blue, orange, yellow, and gray spheres are all schematic representations of the ground state vibrating. As the external field variable a approaches the phase transition point a_0, the curvature of both the first- and second-order phase transitions decreases, but in the second-order phase transition, the curvature becomes negative and the phase transition is spontaneous, while in the first-order phase transition, the phase transition overcomes the reduced potential barrier and enters the final state. The decrease in curvature corresponds to the softening of the lattice frequency.

Table 1.1 Crystal structure of β-phase [9] and λ-phase [8] of Ti_3O_5

	β-Ti_3O_5	λ-Ti_3O_5
Space Group	C 2/m	C 2/m
a(Å)	9.752(1)	9.8378(5)
b(Å)	3.8020(5)	3.78674(11)
c(Å)	9.442(1)	9.9707(3)
β(degree)	91.55(1)	91.257(3)
Ti1	(0.1280(4), 0.0000, 0.0440(4))	(0.6299(4), 0.0000, 0.0522(2))
Ti2	(0.7786(4), 0.0000, 0.2669(4))	(0.3055(2), 0.0000, 0.2462(4))
Ti3	(0.0538(4), 0.0000, 0.3659(4))	(0.6347(4), 0.0000, 0.4352(2))
O1	(0.676(3), 0.0000, 0.060(2))	(0.1795(8), 0.0000, 0.0657(8))
O2	(0.241(3), 0.0000, 0.245(3))	(0.7343(8), 0.0000, 0.2487(7))
O3	(0.588(2), 0.0000, 0.345(2))	(0.1935(8), 0.0000, 0.4285(7))
O4	(0.953(2), 0.0000, 0.158(2))	(0.5468(8), 0.0000, 0.8732(7))
O5	(0.866(2), 0.0000, 0.441(2))	(0.4519(9), 0.0000, 0.3872(7))

Chapter 2　Electronic structure calculations of β- and λ-phases of Ti_3O_5

本章は雑誌等にて公開予定のため、非公開とする。

Chapter 3　Calculation of the phase transition from β-phase to λ-phase by molecular dynamics

3.1 Introduction for this chapter

In Chapter 2, we discussed the possibility of inducing a phase transition from β-phase Ti_3O_5 to λ-phase by applying a lattice elongation to the *c*-axis. The purpose of this chapter is to verify whether the phase transition can be actually observed by molecular dynamics, and to evaluate the structural change and electronic state during the phase transition.

3.2 Simulation of phase transition by *ab-initio* molecular dynamics

本節は雑誌等にて刊行予定のため、非公開とする。

3.3 Classical molecular dynamics

In section 3.2, we discussed the observation of the phase transition from β-phase to λ-phase due to tensile strain in the *c*-axis direction by first-principles molecular dynamics. However, for a more experimental setting, it is more appropriate to perform the calculations in an ensemble with controlled stresses. In addition, since the experimentally reported phase transitions between β- and λ-phases are first-order phase transitions, in reality, the phase transitions are expected to proceed in the form of nucleation and growth, starting from nuclei generated by phase transitions in some of the multiple unit lattices. Since it is difficult to reproduce this mode of phase transition in a single lattice calculation, it is appropriate to use a larger number of supercells in the calculation. In this section, we will discuss the stress control calculation under the supercell by the classical molecular dynamic method.

3.3.1 Calculational method

The calculations in this section were performed with the calculation code LAMMPS (Large-scale Atomic/Molecular Massively Parallel Simulator) [89]. As in Chapter 2, the series of calculations are performed on the computation support virtual OS "Materi Apps Live! (Ver. 3.2)". The Nos’e-Hoover method was applied for temperature control, and the Parrinello-Rahman barostat was applied for stress control, both are implemented in LAMMPS. LAMMPS requires to specify an empirical or semi-empirical potential to obtain the interatomic potential. As mentioned in Chapter 2, Ti_3O_5 has different effective charges between different inequivalent sites, making it difficult to apply a simple ionic potential. Therefore, COMB3, the third generation of the semi-empirical charge transfer many-body potential, COMB (Charge Optimized ManyBody) potential, was used in the calculations of this section [90-92].

3.3.2 Construction of a model for calculation

The computational model was set to a supercell with the unit lattice extended to multiple periods along the crystal lattice axis. This was done firstly to satisfy the requirement that the COMB3 potential used in the calculations be at least twice as large as the specified potential cutoff radius, and secondly to enable observation of the phase transition from nucleation to evolution when dealing with molecular dynamics of first-order phase transitions. In the case of molecular dynamics and lattice dynamics, when the number of calculated atoms is large, the calculation cost is enormous if all the interatomic potentials are included in the calculation. Therefore, in order to reduce the cost, a parameter of distance is introduced to handle interactions only with atoms that are within a certain distance of the target atom. The distance at which this interaction is included in the calculation corresponds to the cutoff radius. If the supercell is less than twice the size of the cutoff radius, *i.e.*, the supercell is smaller than the size of the cutoff sphere, and the supercell has a periodic boundary, the cutoff sphere that exceeds the area of the supercell will move to the opposite end of the supercell due to the periodic boundary, the cutoff spheres will overlap, and the interaction with the atoms in the overlapped area will be calculated. The interaction is calculated twice, and the calculation cannot be done properly. Therefore, one side of the supercell must be larger than twice the cutoff radius.

Based on the lattice constants and fractional coordinates of the conventional cell consisting of 32 atoms of $Ti_{12}O_{20}$ obtained from a previous report [8], the supercell containing 8000 atoms was prepared by extending the crystal lattice by 5, 10, and 5 periods in the *a*-, *b*-, and *c*-axis directions, respectively (Figure 3.11). The boundary of the supercell was determined to be a periodic boundary condition, with a cutoff radius of 15.5 Å for the COMB3 potential for Ti and O, so that one side of the supercell should be greater than 31 Å and the anisotropy should be low. Spatial symmetry or tuning of the behavior of each inequivalent site for the entire system was not set, but they were treated as a P1 symmetry of 8000 atoms. The real-space basis vectors of the supercell are defined as 3*3 matrices, and in this study, the axial components of β- and λ-phase Ti_3O_5 are specified by the matrix (3.1) as a Trigonal Prism type, since both phases are monoclinic crystal structure (C2/m).

$$\begin{bmatrix} L_{xx} & 0 & 0 \\ L_{xy} & L_{yy} & 0 \\ L_{xz} & L_{yz} & L_{zz} \end{bmatrix} \quad (3.1)$$

Here, L_{ij} ($i, j=x, y, z$) are all numerical components. the first basic lattice vector of the Trigonal lattice is set to be parallel to the *X*-axis, the second vector is defined in the *XY*-plane, and the third vector is defined in *XYZ*-space. If the second vector is non-parallel to the *Y*-axis (*i.e*., non-orthogonal to the *X*-axis), then the shear component *XY* is defined in the *XY*-plane in the direction of the *X*-axis. Similarly, for the third vector, the degree of non-parallelism with the *Z* axis is controlled by the shear components L_{yz} (in the *YZ* plane, in the *Y* direction) and L_{xz} (in the *XZ* plane, in the *X* direction). In the calculation, the stresses are applied with respect to a global right-handed Cartesian coordinate system in the software. The *c*-axis of the supercell (crystal lattice) is aligned with the *X*-axis of this Cartesian coordinate system, and the *b*-axis is aligned with the *Z*-axis. In β-phase crystal lattice, the *a*-axis is orthogonal to the *b*-axis but non-orthogonal to the *c*-axis, so the *y*-axis and *a*-axis are not aligned. Each stress component corresponds to Eq. (3.1) and is controlled for the six components shown in the matrix (3.2), except for the three non-diagonal components whose length components are defined as zero. (The uncontrolled component in the matrix was set to -.)

$$\begin{bmatrix} \sigma_{xx} & - & - \\ \sigma_{xy} & \sigma_{yy} & - \\ \sigma_{xz} & \sigma_{yz} & \sigma_{zz} \end{bmatrix} \quad (3.2)$$

3.3.3 Structural relaxation of β-phase Ti_3O_5

In order to obtain a reference supercell for a series of calculations, we first performed the structural relaxation of β-phase Ti_3O_5 in classical molecular dynamics.

The first step of the structural relaxation is the optimization of the effective charge for the experimental lattice parameter at room temperature (Table 1.1), and then the charge configuration is maintained by the NPT ensemble at 300 K and atmospheric pressure. The effective charge of Ti is +1.90 *e* according to a previous report [93], which calculated the rutile-type titanium dioxide TiO_2 using the COMB potential, and the effective charge of O is estimated to be about -0.95 *e* assuming the neutrality of the system. These values are very close to the Bader effective charge mentioned in Chapter 2. Assuming that the chemical formula Ti_3O_5 is charge neutral, the total effective charge of Ti(1)-(3) sites is expected to be about +5 *e*. In addition, although the structure of λ-phase Ti_3O_5 is distorted from that of α-phase, the Ti(1) and Ti(3) sites are relatively close to each other, and the effective charge of only Ti(2) is expected to be inequivalent. In this study, we set the charge configuration balance similar to that of λ-phase structure as the initial value, and as shown in Table 3.1, we set Ti(2) to be inequivalent. For the oxygen sites, all sites were set equal to -1 *e*.

From here, charge relaxation was performed using the QEQ method [94] to minimize the potential energy of the system at absolute zero. For the relaxation, the lattice constant was kept constant, and the charge and the coordinates of the atoms were allowed to change. Since the charge configurations of the optimized inequivalent atomic sites were identical among the unit cells in the supercell, only the charges after relaxation of the eight inequivalent sites are listed in Table 3.1. λ-structure, which was optimized by the same procedure, is also shown in Table 3.1. The effective charge at each Ti site is indeed larger in β-phase, reflecting the strong inequivalence of the structure. Although there is a difference of the order of 0.1 *e* with the Bader effective charge obtained by the first principle calculation, qualitatively, it is confirmed that the effective charges tend to be the same, and the optimum value is found to be reliable.

Next, the supercell was subjected to structural relaxation in terms of lattice parameters and atomic coordinates by calculating 1 fs/step × 10000 steps in the NPT ensemble at a control temperature of 300 K. The stress component was calculated in the computational space.

The stress components were controlled to maintain 0 Bar(=0 GPa) for the *X* component σ_{XX}, *Y* component σ_{YY}, *Z* component σ_{ZZ}, and the shear component σ_{XY} with respect to the *X*-axis direction of the *a*-axis in the conventional cell, while the remaining shear components σ_{YZ} and σ_{XZ} were controlled to maintain 0 Bar for the *Y*-axis and *Z*-axis For the remaining shear components σ_{YZ} and σ_{XZ}, the shear amounts *YZ* and *XZ* are always set to 0, not the stress, so that the *Y* and *Z* axes and the *X* and *Z* axes remain orthogonal from the crystal lattice structure. The lattice parameters of the obtained unit lattice were a=9.862 Å, b=4.051 Å, c=9.256 Å, and β=91.70° on average (Figure 3.12). Thereafter, this supercell was set as the initial structure, and calculations on phase transitions such as strain and stress application and temperature control were performed.

3.3.4 NVT ensemble under fixed strain

In order to calculate the phase transition behavior, we first attempted to reproduce the NVT ensemble obtained in section 3.2. We started the calculation with the supercell relaxed in section 3.3.3 under a predetermined amount of tensile strain in the *c*-axis direction, and investigated the atomic behavior through the time evolution of the NVT ensemble. A snapshot of the entire supercell after 5000 steps is shown in Figure 3.13. The snapshot of the whole supercell after 5000 steps is shown in Figure 3.13. When the strain is small, some lattices remain in β-phase or in the intermediate state between β-phase and λ-phase, but when the tensile strain is more than 6 %, the whole cell transitions to λ-phase structure. From these results, it can be concluded that not only by AIMD but it is also possible to observe the phase transition from β-phase to λ-phase computationally using classical molecular dynamics calculations, and further calculations will be discussed below.

3.3.5 Calculation under continuously stress-inducing condition

When investigating the behavior of a specimen under uniaxial stress or application, it is common to experimentally fix both ends of the specimen to an apparatus and deform the specimen by moving the fixture. Therefore, the calculations in this section are based on this setup. For the initial structure, the controlled stress is applied to one axis of the *X*-axis from 0 Bar (=0 GPa) to 60000 Bar (=6 GPa) at a constant acceleration of 6 Bar/step for 1 (fs/step) × 10000 steps. In Step 0, the kinetic energy was randomly applied to the entire system, corresponding to an initial velocity of 300 K. The temperature of the system was kept constant at 300 K during the calculation. 0 Bar is maintained for the unstressed components σ_{yy}, σ_{zz}, and σ_{xy}, and no stress control is applied to σ_{yz} and σ_{xz} as in the structural relaxation calculation, so that the shear displacement in the lattice is always zero. The charge was kept constant during the calculation. In the calculation results, the phase transition is confirmed when stress is applied to the *c*-axis (Figure 3.26), and qualitatively the results are consistent with the prediction based on the potential curve mentioned in Chapter 2. The evolution of the main thermodynamic parameters obtained during the calculations is shown in Figure 3.28. The temperature was kept around 300 K, and the difference is within 10 K at most, suggesting that the temperature is well controlled. The strain in each axis shows linear response up to about 7500 steps, which is considered to be in the range of elastic behavior in β-phase, while significant elongation of the *c*-axis and contraction of the *b*-axis occur around 8000 steps, corresponding to the change in the lattice parameter between β-phase and λ-phase. In addition, the *c*-axis length and volume reached a maximum at 8500 steps and then converged to a slightly lower value, suggesting that the phenomenon is similar to the volume maximization observed in the photo-induced phase transition [34].

Simultaneously with the change in axial length, the *β*-angle decreased to less than 90° and then increased again to higher than 90° (Figure 3.28(c)). This indicates that in the intermediate state, an inversion of crystallographic *b*-axis has occurred, and it recovered as the phase transition completed. As for the *c*-axis length and tensile stress, the maximum tensile strain was about 2 %, indicating elastic behavior. This is in good agreement with the potential curve (Figure 2.3) shown in Chapter 2, where the contact point that gives the isoenthalpy line between β- and λ-phases, *i.e.* the strain at which the phase transition is expected to start, is 2 % tensile strain from the reference lattice constant in β-phase. The stress range in which the phase transition occurs is 4.5 GPa~6.0 GPa, which is intermediate between the estimates given in Chapter 2 with and without the onsite Coulomb interaction. The sequence of behaviors was completed in about 2000 steps (=2000 fs) of 7500~9500 steps, which is comparable to the time scale of phase transitions recently observed in photo-induced phase transitions [34].

In order to discuss the movement of individual atoms with time evolution in more detail, first the change in interatomic distances between the Ti(3) site and the O(3) and O(4) sites, which are the most characteristic features of the structural change, are shown in Figure 3.28(e) and Figure 3.29. Although a supercell contains 1000 atoms of Ti(3) sites, we sampled two sites per conventional cell, for a total of 500 sites, and show the average value and the standard deviation assuming normal distribution. The distance between Ti(3) and O(3) sites in the *ac*-plane was evaluated as the degree of phase transition, because it has large difference between β-phase and λ-phase. During the calculation, an increase in the Ti(3)-O(4) interatomic distance and a decrease in the Ti(3)-O(3) interatomic distance were observed at 7500~9500 steps. The former is consistent with the dissociation of Ti(3)-O(4) bonds and the latter with the formation of Ti(3)-O(3) bonds, which together correspond to the coordination change of oxygen around the Ti(3) site during the phase transition. This displacement occurs at the same time as the abrupt change in the lattice parameter shown in Figure 3.28(b), suggesting that the phase transition is a displacement-type structural phase transition caused by the synchronization of both phenomena.

The snapshots of the supercell obtained in the calculation are shown in Figure 3.14 after 5000 steps, Figure 3.15 for 7000 steps, and Figure 3.16~3.26 for every 250 steps (250 fs) from 7500 to 10000 steps. Initially, the Ti(3) and O(5) sites undergo a slight in-plane displacement in the whole cell from 8000 steps, and the structure enters the intermediate state between β- and λ-phases. After that, the displacement progressed step by step in each cell, and the structure converged from the intermediate state to λ-phase coordination structure. In the series of displacements, the dissociation of Ti(3) from O(4), the approach to O(3) in the plane, and the displacement of O(5) in the *ac*-plane occur synchronously, and can be interpreted as the rotational displacement in the ac plane of the four-atom ring structure consisting of two sites. The direction of rotation is to the right as shown by arrows in Figure 3.20. In this case, the surrounding atoms are slightly attracted to Ti(3) and O(3), which causes negative *XY* shear deformation of the whole lattice and a temporary decrease in the *β*-angle. In other words, in the NPT ensemble in this section, the shear stress σ_{xy} is set to 0 Bar, so there is a degree of freedom for this shear, but if this degree of freedom is not allowed, a higher stress is expected to be required for the phase transition.

The transition from the intermediate state to λ-phase structure can be observed in the whole cell, as shown in Figure 3.27, where the displacement motion occurs first at one site and then propagates to the neighboring sites in the *a*-axis direction. The parallel structure in the *a*-axis direction consisting of Ti(3) and O(5) sites is sandwiched between the parallel structure consisting of Ti(1) and O(4) sites in the *c*-axis direction (left-right direction in the figure). As a result, the propagation of the displacement in the *c*-axis direction is blocked, and the propagation of the phase transition in the *ac*-plane is inferred to be uniaxial and parallel to the *a*-axis. In the snapshots taken at the same time, the positions of Ti(3) and O(5) in the ac plane in the *b*-axis direction (depth direction on the paper) do not differ significantly, suggesting that the propagation speed of the atomic displacements associated with the phase transition is fastest in the *b*-axis, followed by the *a*-axis, and does not occur in the *c*-axis direction, suggesting that the propagation is accompanied by strong anisotropy. This suggests that the propagation is accompanied by strong anisotropy. Since the calculations in this section deal with a population of atoms that are not bound by symmetry, we can observe the onset of displacement at one site and its propagation to surrounding sites, which corresponds to nucleation and expansion in the first-order phase transition. The time required to complete the above phase transition in the whole cell is about 7500 to 10000 steps, or 2.5 ps, which is comparable to the ps order of the time scale in the photo-induced phase transition [34].

3.3.6 Phase transition from β-phase to λ-phase by increasing temperature.

雑誌等にて刊行予定のため、非公開とする。

3.4 Conclusion for this chapter

雑誌等にて刊行予定のため、非公開とする。

第 3 章内 3.2 節に関する図版は雑誌等にて刊行予定のため、非公開とする。

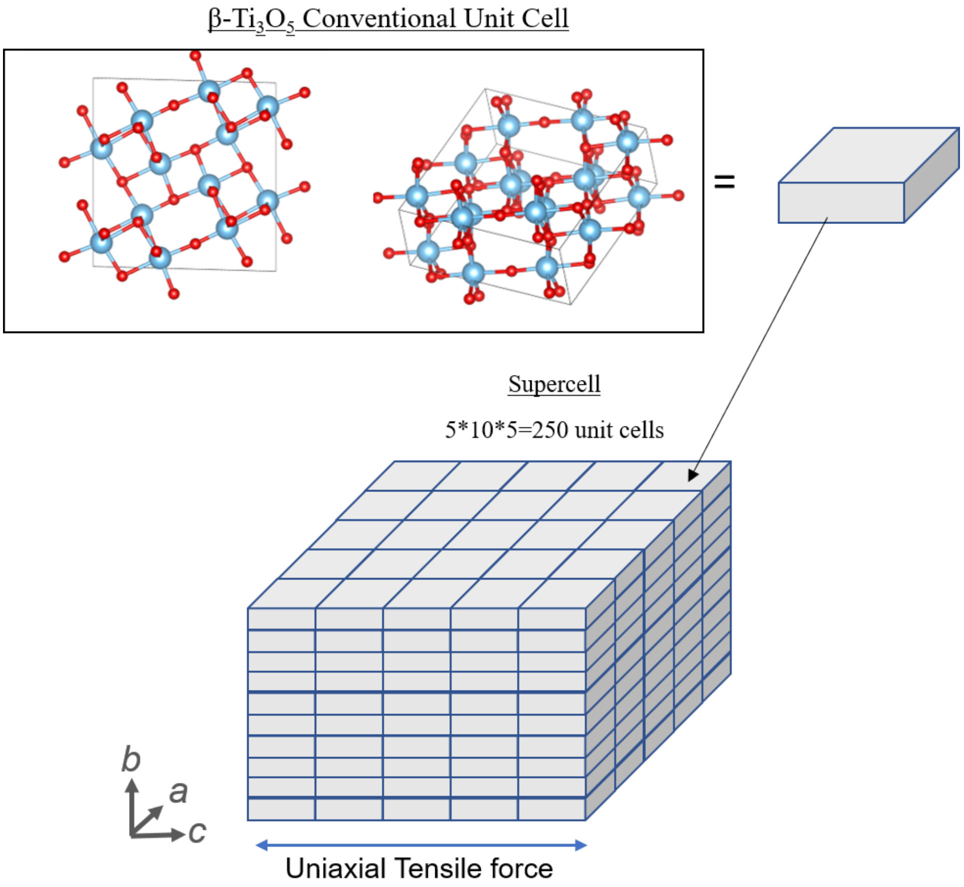
β-Ti3O5 Conventional Unit Cell
=
Supercell
5*10*5=250 unit cells
b
a
c
Uniaxial Tensile force

Figure 3.11 Schematic image for model of the 8000-atom supercell consists of 250 conventional unit cells for classical molecular dynamics calculations.

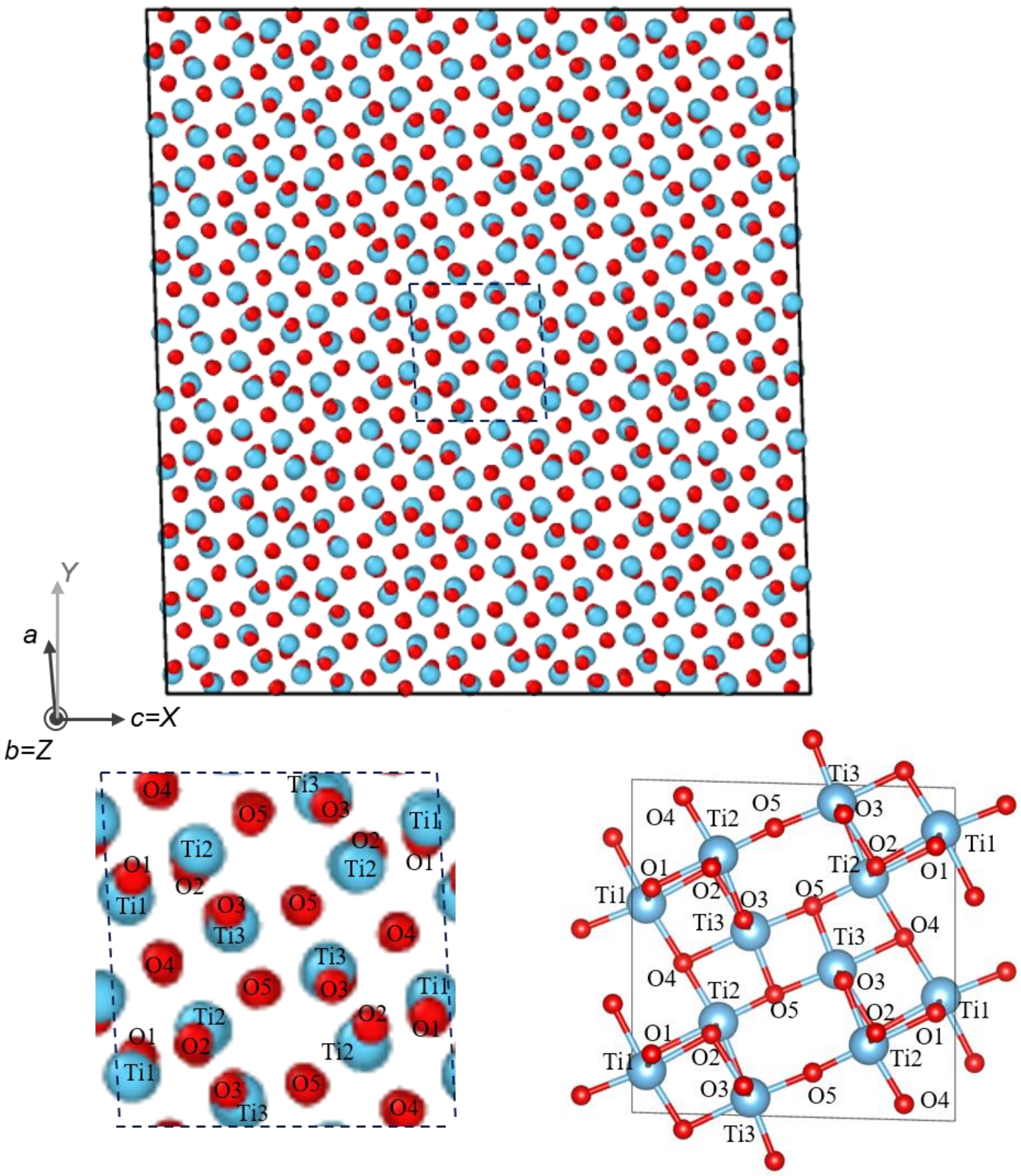
Y
a
c=X
b=Z
O4
Ti3
O5
O3
Ti1
Ti2
O2
O1
Ti2
O1
Ti1
O2
O3
Ti3
O5
O4
Ti3
O5
O3
Ti1
O4
Ti2
O2
O1
O1
O2
Ti1
Ti2
O3
O5
O4
Ti3
O1
O4
Ti2
O5
Ti3
O3
O2
Ti1
Ti2
O1
Ti1
O2
O3
O5
Ti3
Ti3
O4
O4
Ti2
O5
O3
O2
Ti1
O1
O1
Ti1
O2
O3
O5
Ti2
O4
Ti3

Figure 3.12 β-phase Ti$_3$O$_5$ supercell after 10000 steps of structural relaxation in the NPT ensemble at 300 K, σ_{xx}= 0 Bar, σ_{yy}= 0 Bar, σ_{zz}= 0 Bar, and σ_{xy}= 0 Bar. (Upper panel) Snapshot of the entire supercell projected in the *b*-axis direction. (Lower left) Enlarged view of the unit lattice ac surface in the blue dashed line in the supercell, where 10 cells are superimposed in the *b*-axis direction. Correspondence of the eight inequivalent Ti(1)~(3) and O(1)~(5) sites is also shown. (bottom right) β-phase Ti$_3$O$_5$ unit lattice unit lattice experimentally obtained at room temperature, projected onto the *ac*-plane. The images are drawn by OVITO [88] and VESTA [74].

Reproduced with permission from T. Takeda, and S. Ohkoshi, Eur. J. Inorg. Chem. doi:10.1002/ejic.202101037 (c)2022 Wiley-VCH GmbH.

Table 3.1 Effective charges optimized by the QEQ method for β-phase and λ-phase Ti_3O_5. Initial values are given as Initial. The unit is elementary charge (*e*).

Reproduced with permission from T. Takeda, and S. Ohkoshi, Eur. J. Inorg. Chem. doi:10.1002/ejic.202101037 (c)2022 Wiley-VCH GmbH.

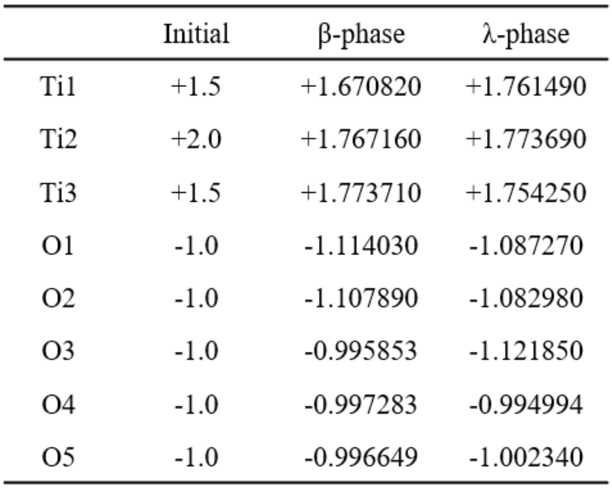

	Initial	β-phase	λ-phase
Ti1	+1.5	+1.670820	+1.761490
Ti2	+2.0	+1.767160	+1.773690
Ti3	+1.5	+1.773710	+1.754250
O1	-1.0	-1.114030	-1.087270
O2	-1.0	-1.107890	-1.082980
O3	-1.0	-0.995853	-1.121850
O4	-1.0	-0.997283	-0.994994
O5	-1.0	-0.996649	-1.002340

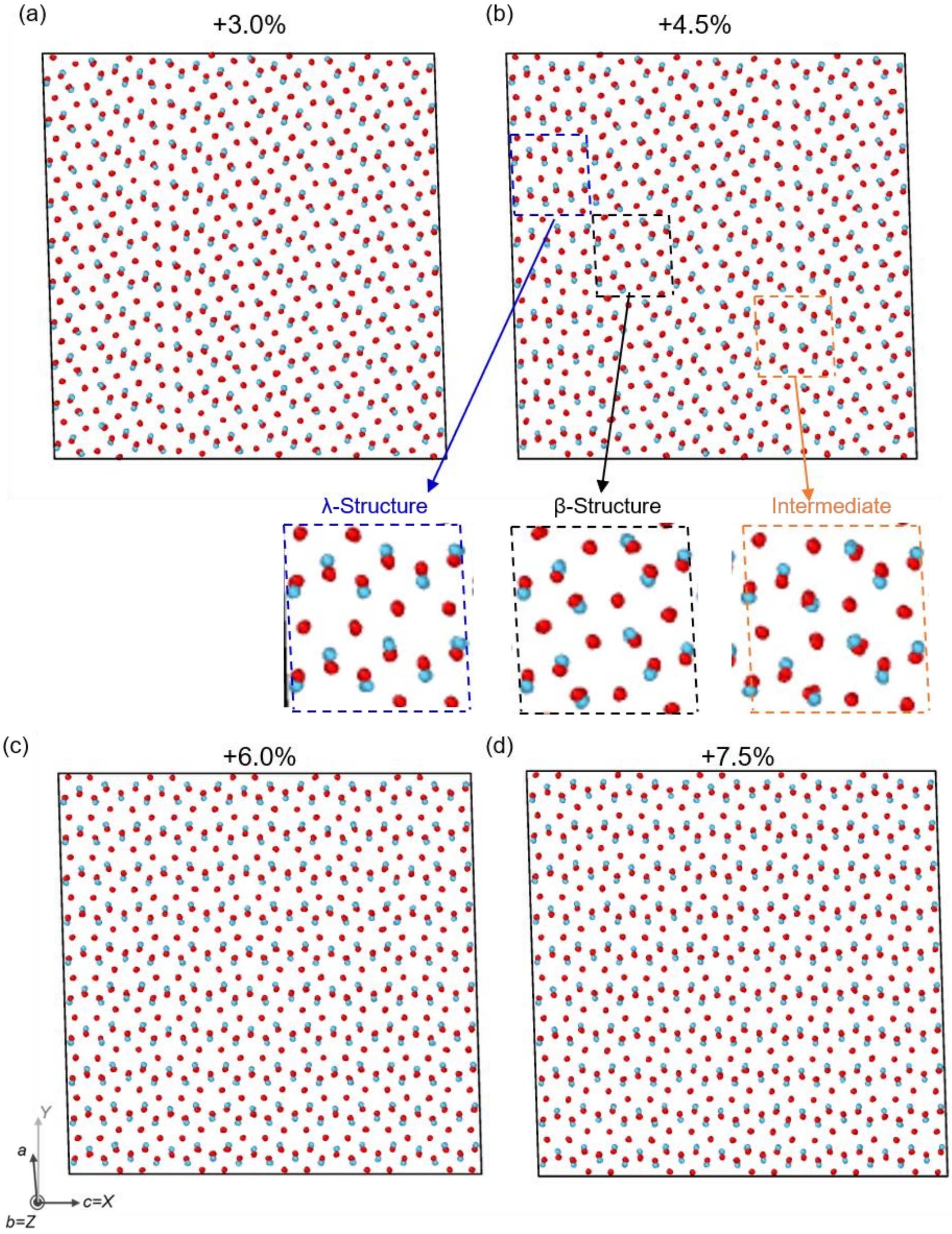

Figure 3.13 Results of NVT ensemble classical molecular dynamics calculations for a β-phase Ti_3O_5 supercell at 300 K under constant tensile strain in the *X*-axis (*c*-axis) direction. The results are shown for (a) 3.0 %, (b) 4.5 %, (c) 6.0 %, and (d) 7.5 %. All the structures are shown after 5000 steps. The light blue and red spheres represent Ti and O atoms, respectively. In (b), the unit lattice corresponding to the λ-phase (blue dashed line), β-phase (black dashed line), and their intermediate (orange dashed line) coordination structures in the supercell is enlarged. The images were drawn by OVITO [88].

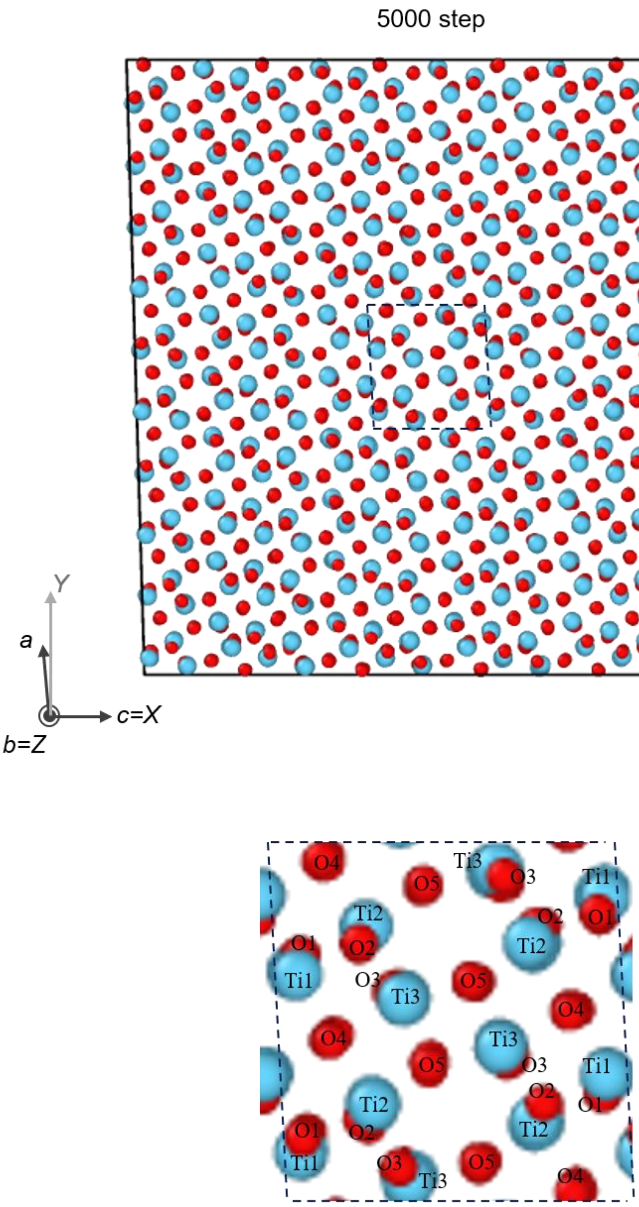
5000 step
Y
a
c=X
b=Z
O4
O5
Ti3
O3
Ti1
Ti2
O2
O1
O1
O2
Ti2
Ti1
O3
Ti3
O5
O4
O4
Ti3
O5
O3
Ti1
O2
O1
Ti2
Ti2
O1
O2
Ti1
O3
Ti3
O5
O4

Figure 3.14 Ti_3O_5 supercell at 300 K, ensemble with tensile stress applied in the *X*-axis (*c*-axis) direction, after 5000 steps (controlled stress 3.00 GPa), and ac plane with *b*-axis perpendicular to the paper plane. The upper panel shows the whole image, and the lower panel shows the area of one cycle in the *a*- and *c*-axis directions, enlarged within the blue dashed line in the upper panel. The light blue and red spheres represent Ti and O, respectively. The bottom row shows the inequivalent eight sites in Ti_3O_5. The image was drawn by OVITO [88].

Reproduced with permission from T. Takeda, and S. Ohkoshi, Eur. J. Inorg. Chem. doi:10.1002/ejic.202101037 (c)2022 Wiley-VCH GmbH.

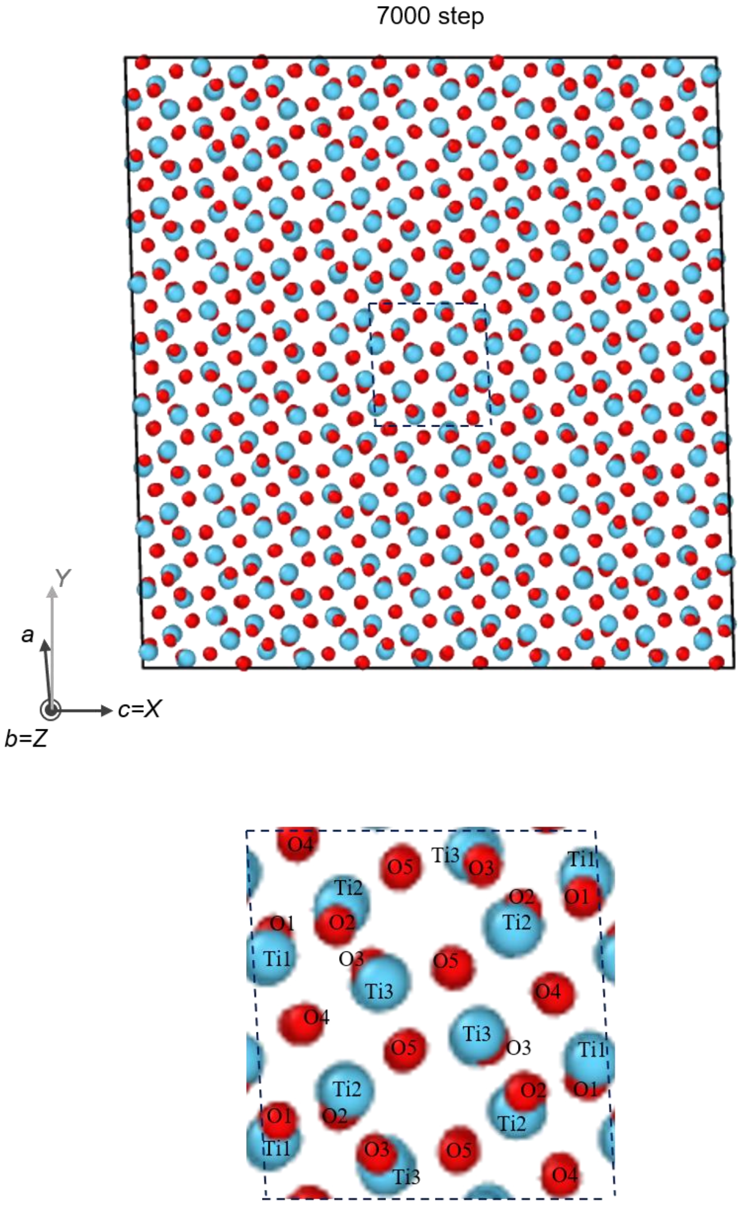
7000 step
Y
a
c=X
b=Z
O4
O5
Ti3
O3
Ti1
Ti2
O2
O1
O1
O2
Ti2
Ti1
O3
O5
Ti3
O4
O4
O5
Ti3
O3
Ti1
Ti2
O2
O1
O1
O2
Ti2
Ti1
O3
O5
O4
Ti3

Figure 3.15 Ti_3O_5 supercell at 300 K, ensemble with tensile stress applied in the *X*-axis (*c*-axis) direction, 7000 steps (controlled stress 4.20 GPa), and *ac*-surface with *b*-axis perpendicular to the paper plane. The upper panel shows the whole image, and the lower panel shows the area of one cycle in the *a*- and *c*-axis directions, enlarged within the blue dashed line in the upper panel. The light blue and red spheres represent Ti and O, respectively. The bottom row shows the inequivalent eight sites in Ti_3O_5. The image was drawn by OVITO [88].

Reproduced with permission from T. Takeda, and S. Ohkoshi, Eur. J. Inorg. Chem. doi:10.1002/ejic.202101037 (c)2022 Wiley-VCH GmbH.

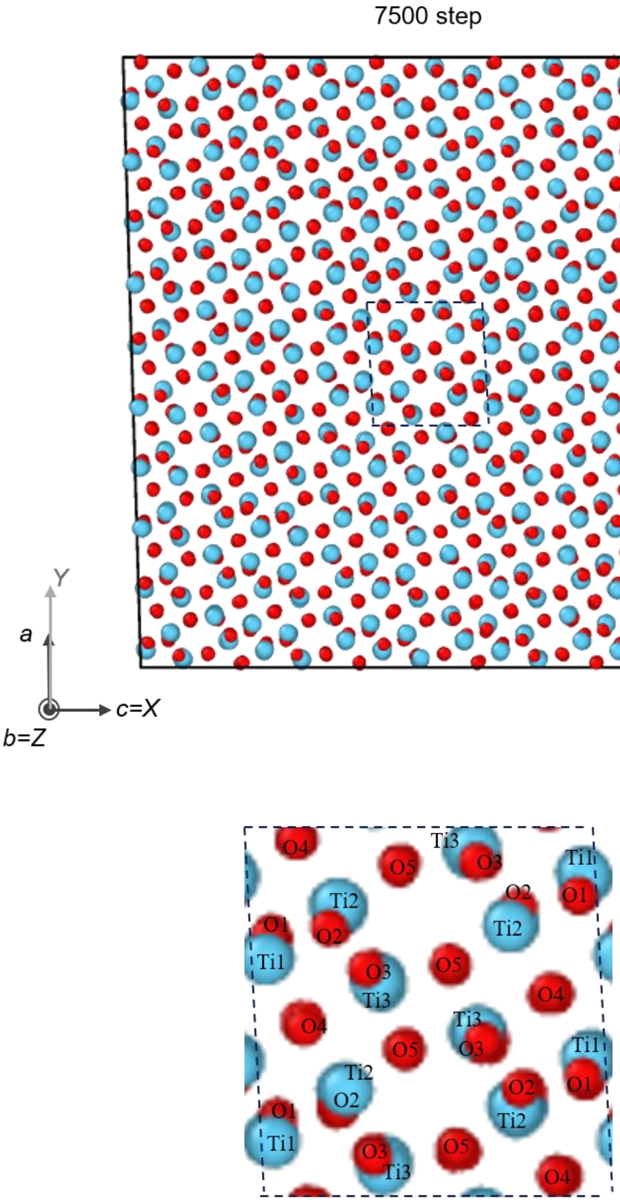
7500 step
Y
a
c=X
b=Z
O4
Ti3
O5
O3
Ti1
Ti2
O2
O1
O1
O2
Ti2
Ti1
O3
Ti3
O5
O4
O4
Ti3
O3
O5
Ti1
O1
Ti2
O2
O2
Ti2
O1
Ti1
O3
Ti3
O5
O4

Figure 3.16 Ti_3O_5 supercell at 300 K, ensemble with tensile stress applied in the *X*-axis (*c*-axis) direction, 7500 steps (controlled stress 4.50 GPa), and *ac*-surface with *b*-axis perpendicular to the paper plane. The upper panel shows the whole image, and the lower panel shows the area of one cycle in the *a*- and *c*-axis directions, enlarged within the blue dashed line in the upper panel. The light blue and red spheres represent Ti and O, respectively. The bottom row shows the inequivalent eight sites in Ti_3O_5. The image was drawn by OVITO [88].

Reproduced with permission from T. Takeda, and S. Ohkoshi, Eur. J. Inorg. Chem. doi:10.1002/ejic.202101037 (c)2022 Wiley-VCH GmbH.

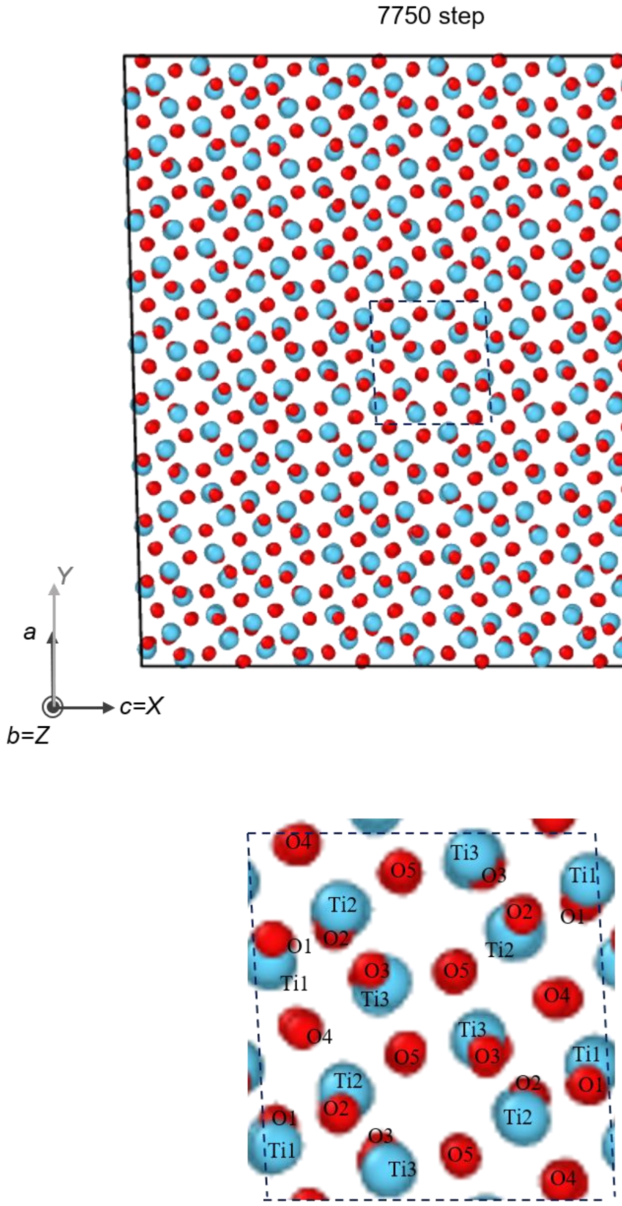
7750 step
Y
a
c=X
b=Z
O4
O5
Ti3
O3
Ti1
Ti2
O2
O1
O1
O2
Ti2
Ti1
O3
O5
Ti3
O4
O4
Ti3
O5
O3
Ti1
Ti2
O2
O1
O2
Ti2
O1
O3
Ti1
Ti3
O5
O4

Figure 3.17 Ti_3O_5 supercell at 300 K, ensemble with tensile stress applied in the *X*-axis (*c*-axis) direction, 7750 steps (controlled stress 4.65 GPa), and *ac*-surface with *b*-axis perpendicular to the paper plane. The upper panel shows the whole image, and the lower panel shows the area of one cycle in the *a*- and *c*-axis directions, enlarged within the blue dashed line in the upper panel. The light blue and red spheres represent Ti and O, respectively. The bottom row shows the inequivalent eight sites in Ti_3O_5. The image was drawn by OVITO [88].

Reproduced with permission from T. Takeda, and S. Ohkoshi, Eur. J. Inorg. Chem. doi:10.1002/ejic.202101037 (c)2022 Wiley-VCH GmbH.

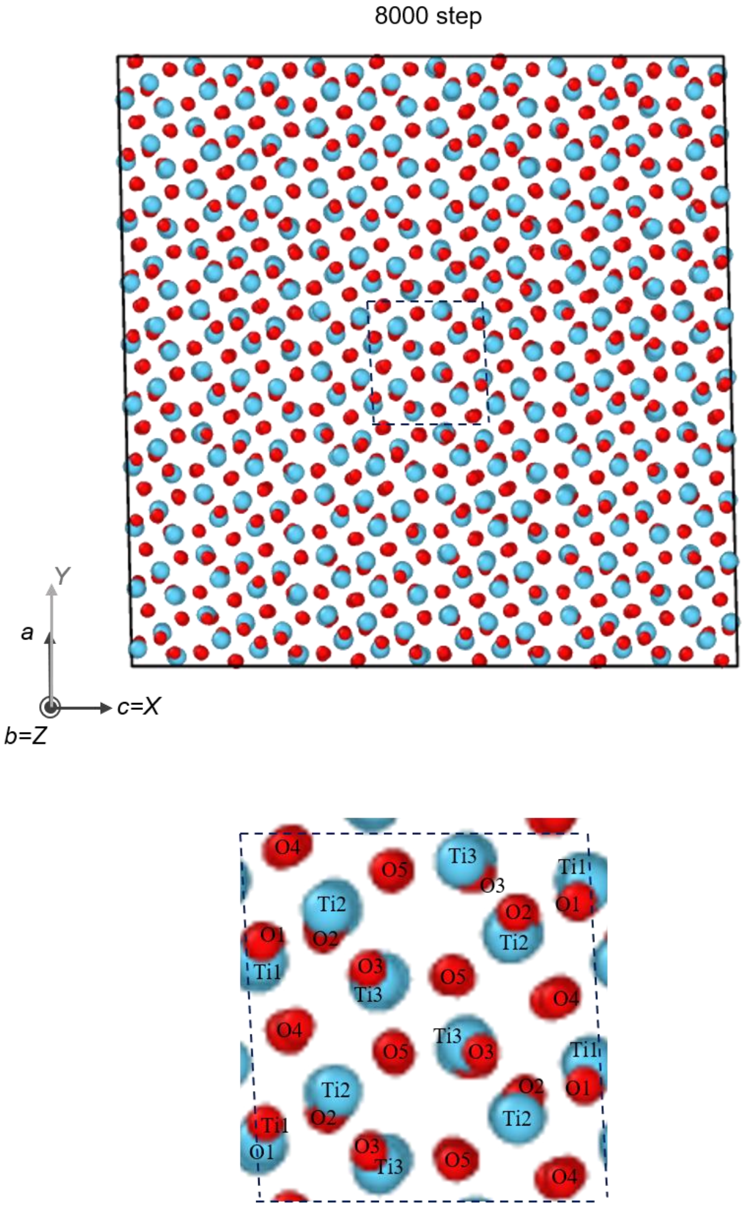
8000 step
Y
a
c=X
b=Z
O4
O5
Ti3
O3
Ti1
O1
Ti2
O2
O2
Ti2
O1
O2
Ti1
O3
Ti3
O5
O4
O4
O5
Ti3
O3
Ti1
O1
Ti2
O2
O2
Ti2
Ti1
O1
O3
Ti3
O5
O4

Figure 3.18 Ti_3O_5 supercell at 300 K, ensemble with tensile stress applied in the *X*-axis (*c*-axis) direction, 8000 steps (controlled stress 4.80 GPa), and *ac*-surface with *b*-axis perpendicular to the paper plane. The upper panel shows the whole image, and the lower panel shows the area of one cycle in the *a*- and *c*-axis directions, enlarged within the blue dashed line in the upper panel. The light blue and red spheres represent Ti and O, respectively. The bottom row shows the inequivalent eight sites in Ti_3O_5. The image was drawn by OVITO [88].

Reproduced with permission from T. Takeda, and S. Ohkoshi, Eur. J. Inorg. Chem. doi:10.1002/ejic.202101037 (c)2022 Wiley-VCH GmbH.

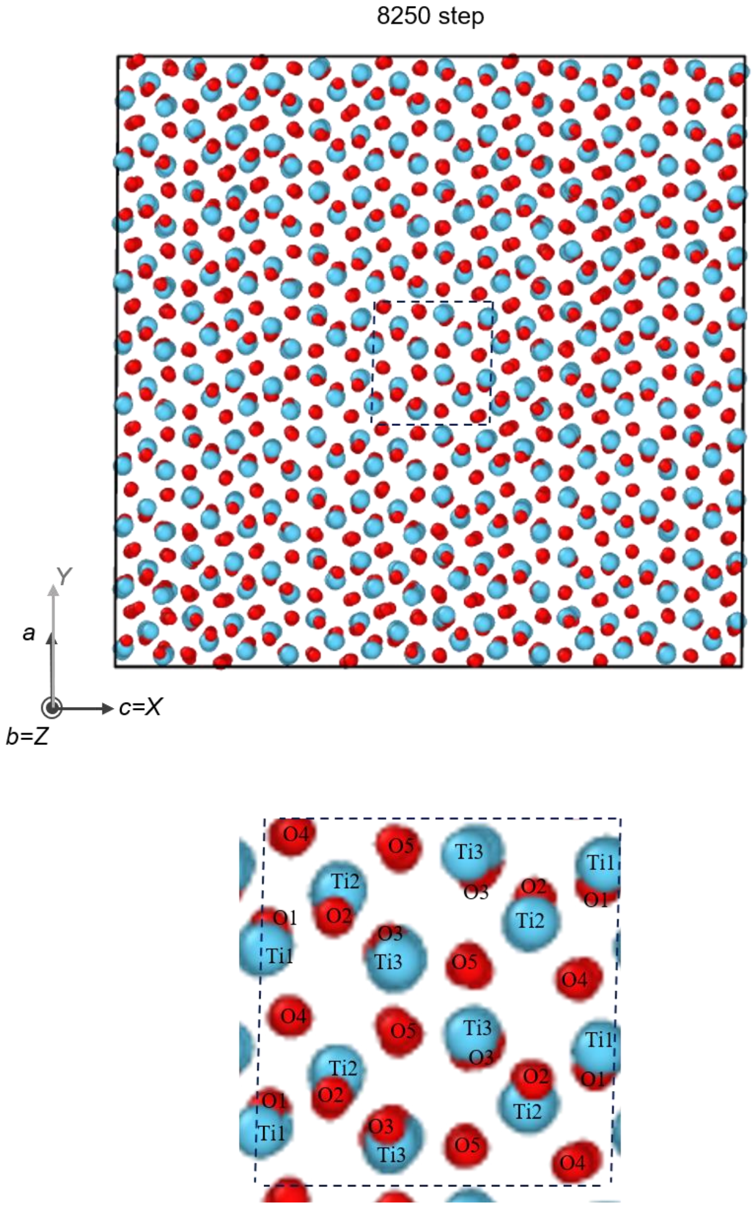
8250 step
Y
a
c=X
b=Z
O4
O5
Ti3
Ti1
Ti2
O2
O3
O1
O1
O2
Ti2
Ti1
O3
Ti3
O5
O4
O4
O5
Ti3
Ti1
O3
Ti2
O2
O1
O1
O2
Ti2
Ti1
O3
Ti3
O5
O4

Figure 3.19 Ti_3O_5 supercell at 300 K, ensemble with tensile stress applied in the *X*-axis (*c*-axis) direction, 8250 steps (controlled stress 4.95 GPa), and *ac*-surface with *b*-axis perpendicular to the paper plane. The upper panel shows the whole image, and the lower panel shows the area of one cycle in the *a*- and *c*-axis directions, enlarged within the blue dashed line in the upper panel. The light blue and red spheres represent Ti and O, respectively. The bottom row shows the inequivalent eight sites in Ti_3O_5. The image was drawn by OVITO [88].

Reproduced with permission from T. Takeda, and S. Ohkoshi, Eur. J. Inorg. Chem. doi:10.1002/ejic.202101037 (c)2022 Wiley-VCH GmbH.

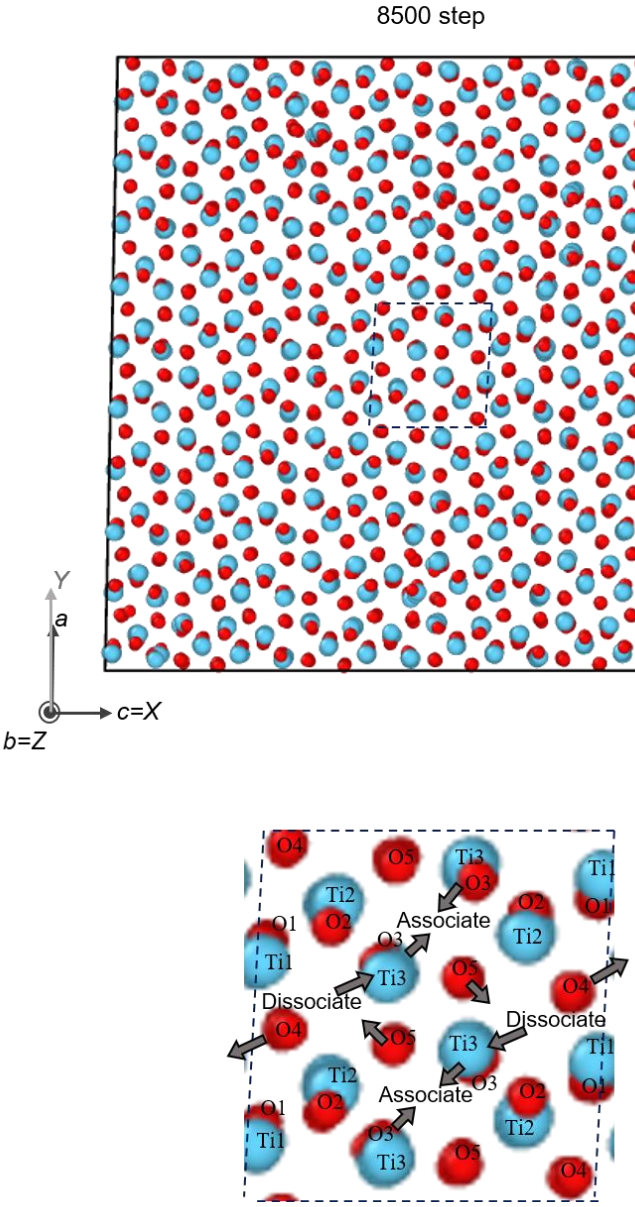
8500 step
Y
a
c=X
b=Z
O4
O5
Ti3
Ti1
Ti2
O3
O2
O1
O1
Associate
O3
Ti2
Ti1
Ti3
O5
O4
Dissociate
O4
O5
Ti3
Dissociate
Ti1
Ti2
O2
Associate
O3
O2
O1
O1
Ti1
O3
Ti2
Ti3
O5
O4

Figure 3.20 Ti_3O_5 supercell at 300 K, ensemble with tensile stress applied in the *X*-axis (*c*-axis) direction, 8500 steps (controlled stress 5.10 GPa), and *ac*-surface with *b*-axis perpendicular to the paper plane. The upper panel shows the whole image, and the lower panel shows the region of one cycle in the a- and c-axis directions, enlarged within the blue dashed line in the upper panel. The light blue and red spheres represent Ti and O, respectively. In the bottom row, the eight inequivalent sites in Ti_3O_5 are also indicated. The gray arrows indicate the direction of displacement of Ti(3) and O(3), O(4), and O(5) sites, which are greatly displaced during the phase transition to the lambda phase. The image was drawn by OVITO [88].

Reproduced with permission from T. Takeda, and S. Ohkoshi, Eur. J. Inorg. Chem. doi:10.1002/ejic.202101037 (c)2022 Wiley-VCH GmbH.

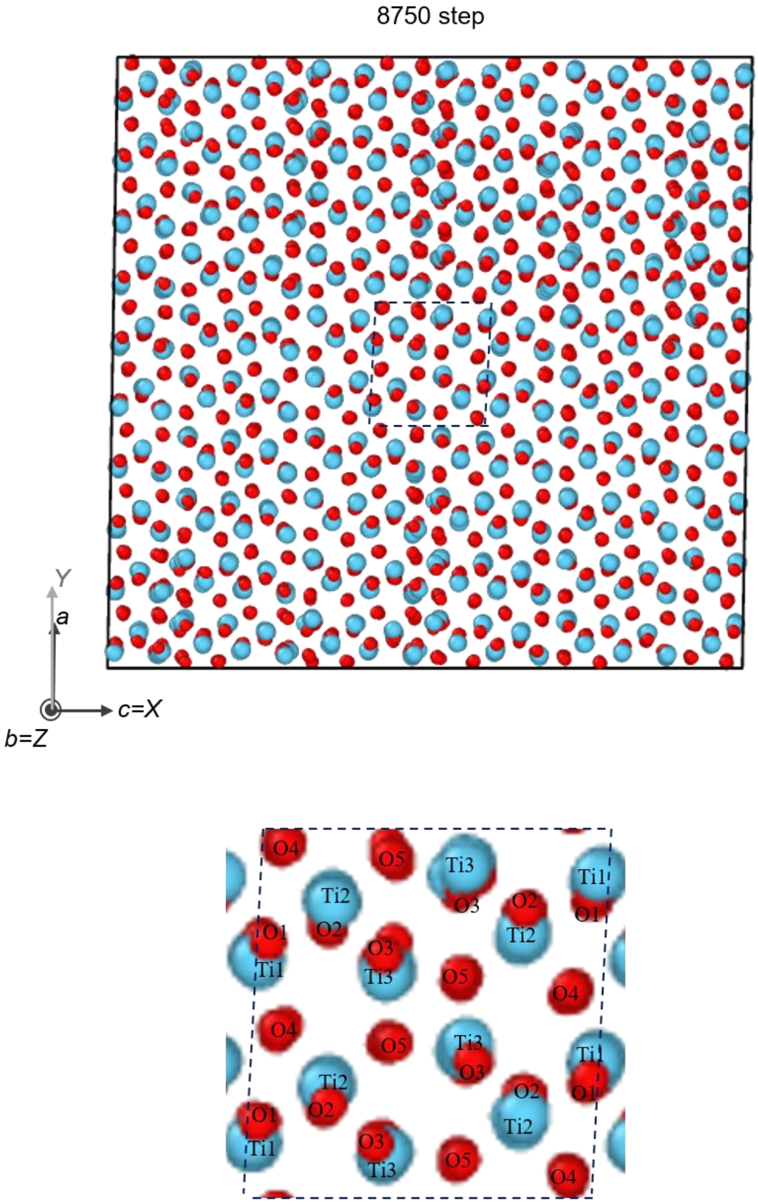
8750 step
Y
a
c=X
b=Z
O4
O5
Ti3
Ti1
Ti2
O3
O2
O1
O1
O2
Ti2
O3
Ti1
Ti3
O5
O4
O4
O5
Ti3
Ti1
Ti2
O3
O2
O1
O1
O2
Ti2
O3
Ti1
Ti3
O5
O4

Figure 3.21 Ti_3O_5 supercell at 300 K, ensemble with tensile stress applied in the *X*-axis (*c*-axis) direction, 8750 steps (controlled stress 5.25 GPa), and *ac*-surface with *b*-axis perpendicular to the paper plane. The upper panel shows the whole image, and the lower panel shows the area of one cycle in the *a*- and *c*-axis directions, enlarged within the blue dashed line in the upper panel. The light blue and red spheres represent Ti and O, respectively. The bottom row shows the inequivalent eight sites in Ti_3O_5. The image was drawn by OVITO [88].

Reproduced with permission from T. Takeda, and S. Ohkoshi, Eur. J. Inorg. Chem. doi:10.1002/ejic.202101037 (c)2022 Wiley-VCH GmbH.

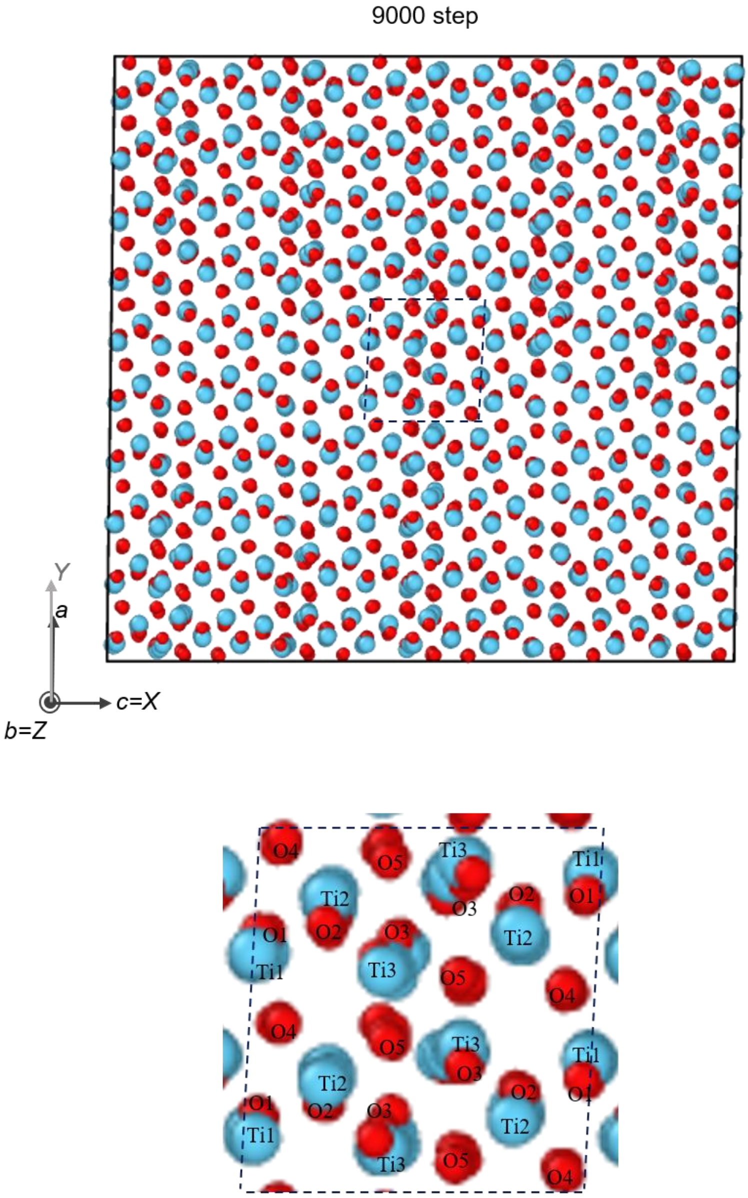
9000 step
Y
a
c=X
b=Z
O4
O5
Ti3
Ti1
Ti2
O3
O2
O1
O1
O2
O3
Ti2
Ti1
Ti3
O5
O4
O4
O5
Ti3
Ti1
O3
O1
Ti2
O2
O2
O1
O3
Ti2
Ti1
Ti3
O5
O4

Figure 3.22 Ti_3O_5 supercell at 300 K, ensemble with tensile stress applied in the *X*-axis (*c*-axis) direction, 9000 steps (controlled stress 5.40 GPa), and *ac*-surface with *b*-axis perpendicular to the paper plane. The upper panel shows the whole image, and the lower panel shows the area of one cycle in the *a*- and *c*-axis directions, enlarged within the blue dashed line in the upper panel. The light blue and red spheres represent Ti and O, respectively. The bottom row shows the inequivalent eight sites in Ti_3O_5. The image was drawn by OVITO [88].

Reproduced with permission from T. Takeda, and S. Ohkoshi, Eur. J. Inorg. Chem. doi:10.1002/ejic.202101037 (c)2022 Wiley-VCH GmbH.

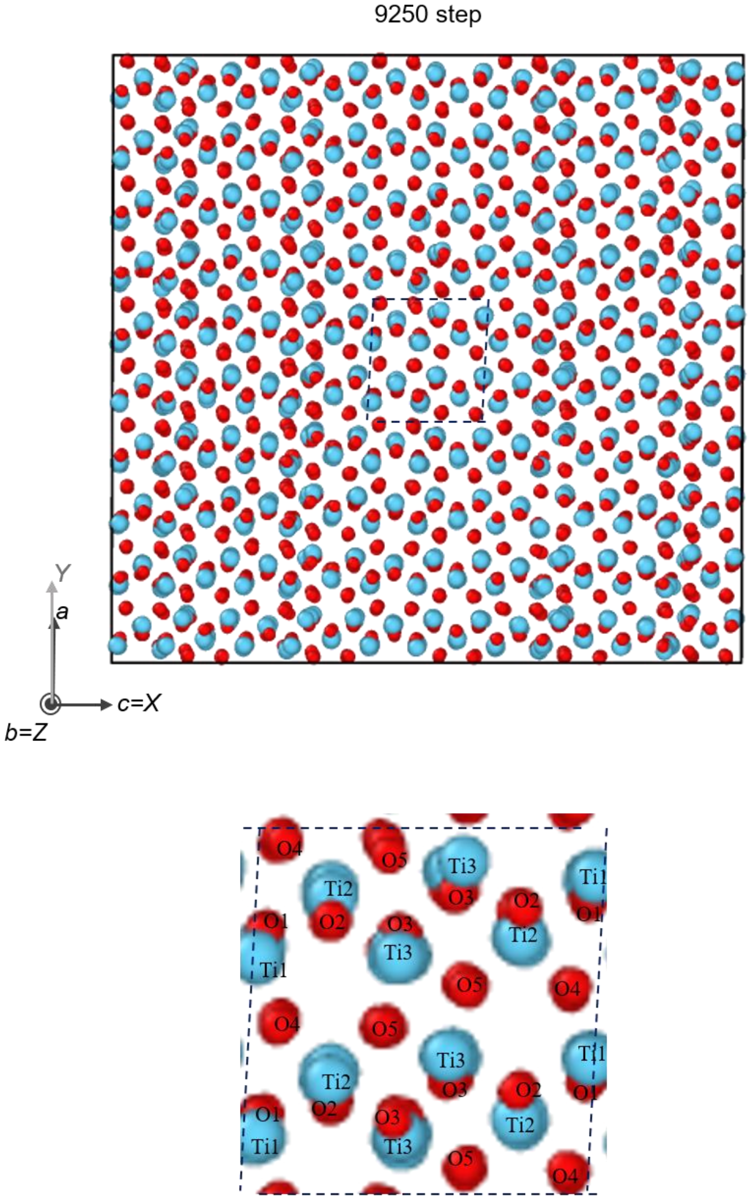
9250 step
Y
a
c=X
b=Z
O4
O5
Ti3
Ti2
Ti1
O3
O2
O1
O1
O2
O3
Ti3
Ti2
Ti1
O5
O4
O4
O5
Ti3
Ti2
Ti1
O3
O2
O1
O1
O2
O3
Ti3
Ti2
Ti1
O5
O4

Figure 3.23 Ti_3O_5 supercell at 300 K, ensemble with tensile stress applied in the *X*-axis (*c*-axis) direction, 9250 steps (controlled stress 5.55 GPa), and *ac*-surface with *b*-axis perpendicular to the paper plane. The upper panel shows the whole image, and the lower panel shows the area of one cycle in the *a*- and *c*-axis directions, enlarged within the blue dashed line in the upper panel. The light blue and red spheres represent Ti and O, respectively. The bottom row shows the inequivalent eight sites in Ti_3O_5. The image was drawn by OVITO [88].

Reproduced with permission from T. Takeda, and S. Ohkoshi, Eur. J. Inorg. Chem. doi:10.1002/ejic.202101037 (c)2022 Wiley-VCH GmbH.

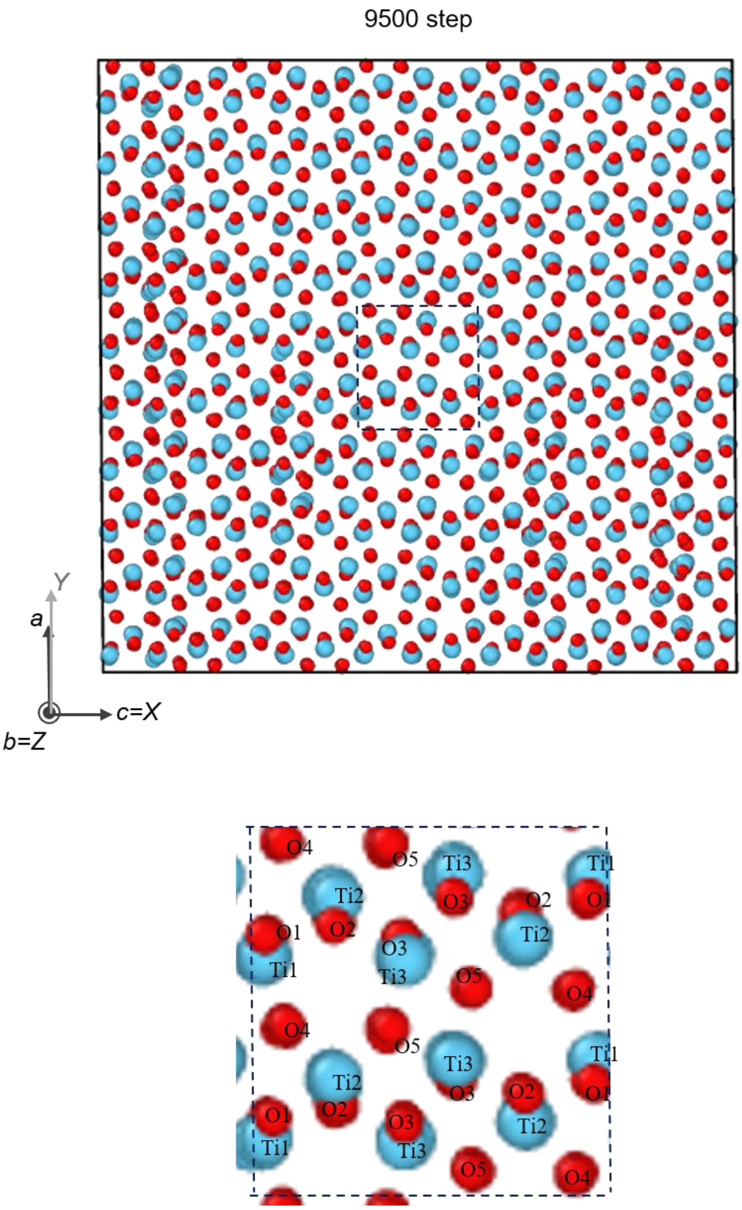
9500 step
Y
a
c=X
b=Z
O4
O5
Ti3
Ti1
Ti2
O3
O2
O1
O1
O2
Ti2
O3
Ti3
O5
O4
O4
O5
Ti3
Ti1
Ti2
O3
O2
O1
O1
O2
O3
Ti2
Ti1
Ti3
O5
O4

Figure 3.24 Ti_3O_5 supercell at 300 K, ensemble with tensile stress applied in the *X*-axis (*c*-axis) direction, 9500 steps (controlled stress 5.70 GPa), and *ac*-surface with *b*-axis perpendicular to the paper plane. The upper panel shows the whole image, and the lower panel shows the area of one cycle in the *a*- and *c*-axis directions, enlarged within the blue dashed line in the upper panel. The light blue and red spheres represent Ti and O, respectively. The bottom row shows the inequivalent eight sites in Ti_3O_5. The image was drawn by OVITO [88].

Reproduced with permission from T. Takeda, and S. Ohkoshi, Eur. J. Inorg. Chem. doi:10.1002/ejic.202101037 (c)2022 Wiley-VCH GmbH.

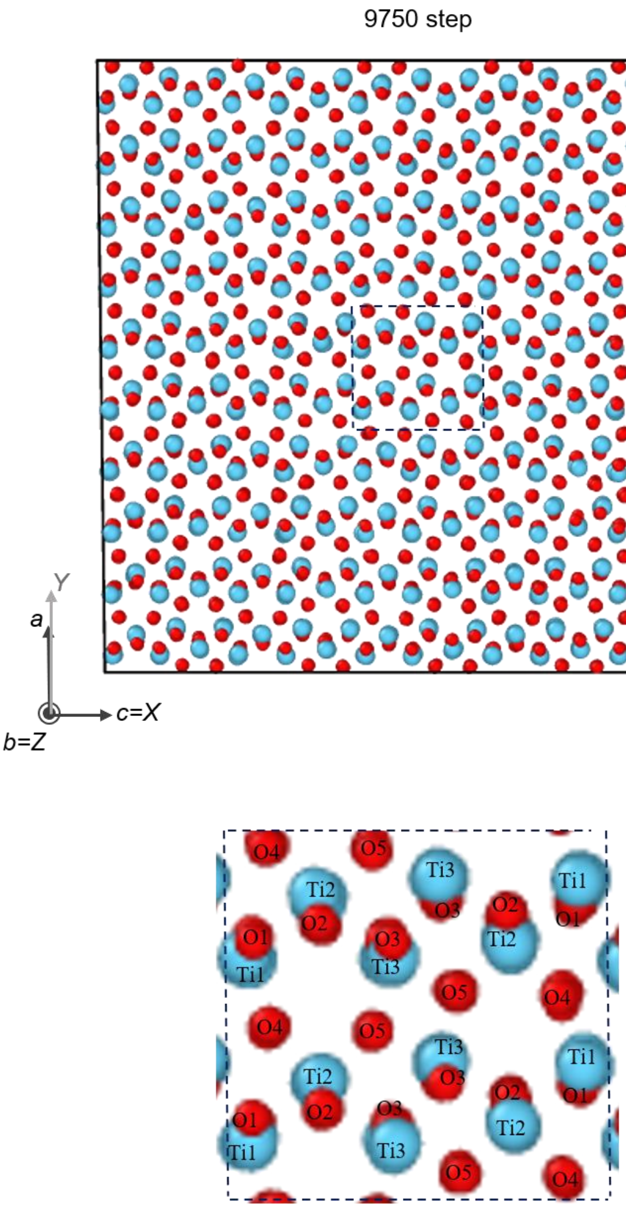
9750 step
Y
a
c=X
b=Z
O4
O5
Ti3
Ti1
Ti2
O3
O2
O1
O1
O2
O3
Ti2
Ti1
Ti3
O5
O4
O4
O5
Ti3
Ti1
Ti2
O3
O2
O1
O1
O2
O3
Ti2
Ti1
Ti3
O5
O4

Figure 3.25 Ti_3O_5 supercell at 300 K, ensemble with tensile stress applied in the *X*-axis (*c*-axis) direction, 9750 steps (controlled stress 5.85 GPa), and *ac*-surface with *b*-axis perpendicular to the paper plane. The upper panel shows the whole image, and the lower panel shows the area of one cycle in the *a*- and *c*-axis directions, enlarged within the blue dashed line in the upper panel. The light blue and red spheres represent Ti and O, respectively. The bottom row shows the inequivalent eight sites in Ti_3O_5. The image was drawn by OVITO [88].

Reproduced with permission from T. Takeda, and S. Ohkoshi, Eur. J. Inorg. Chem. doi:10.1002/ejic.202101037 (c)2022 Wiley-VCH GmbH.

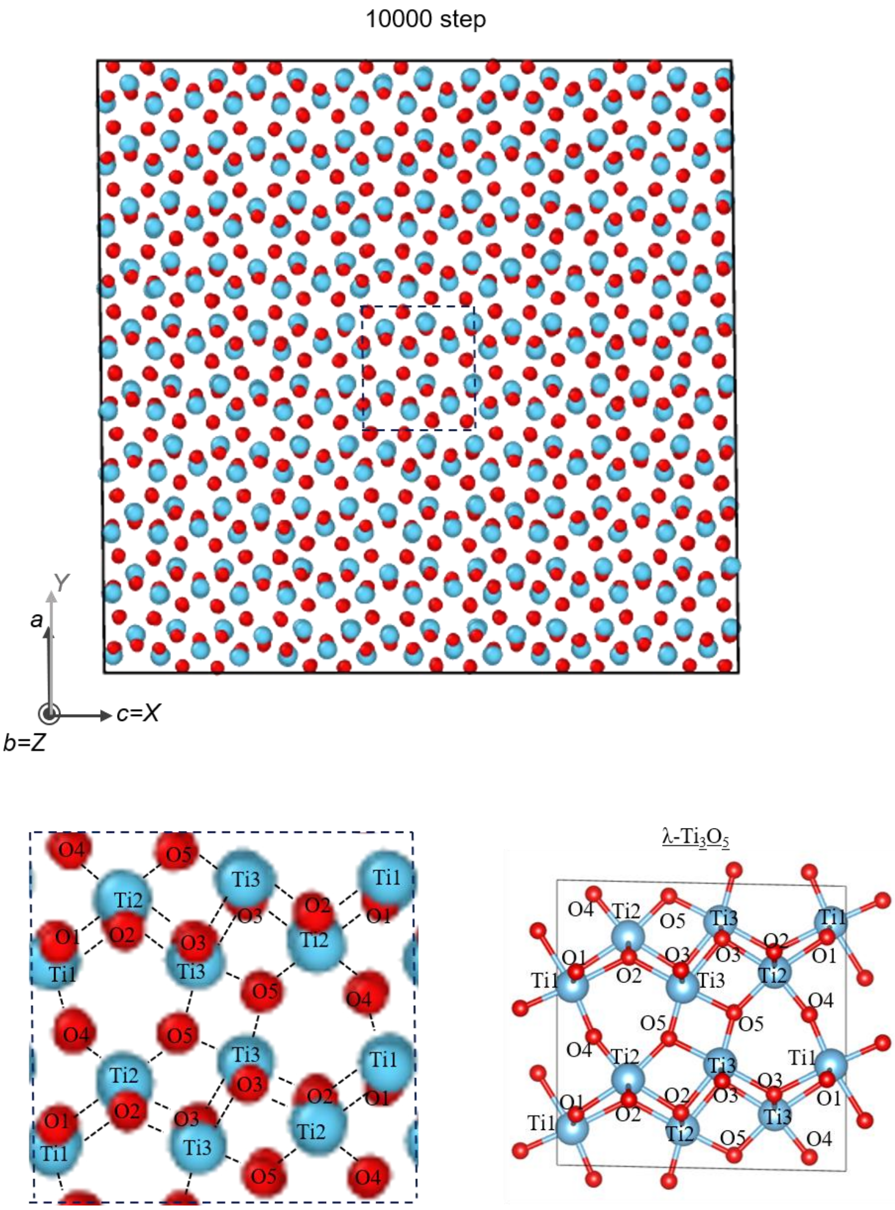

Figure 3.26 Ti_3O_5 supercell at 300 K, ensemble with tensile stress applied in the *X*-axis (*c*-axis) direction, 10000 steps (controlled stress 6.00 GPa), and *ac*-surface with *b*-axis perpendicular to the paper plane. The upper panel shows the whole image, and the lower panel shows the area of one cycle in the *a*- and *c*-axis directions, enlarged within the blue dashed line in the upper panel. The light blue and red spheres represent Ti and O, respectively. In the bottom row, the inequivalent eight sites in Ti_3O_5 are indicated, and the bonds corresponding to the λ-phase structure are indicated by dashed lines. The Conventional Cell of λ-phase Ti_3O_5 is also shown on the right in the bottom row. The image was drawn by OVITO [88].

Reproduced with permission from T. Takeda, and S. Ohkoshi, Eur. J. Inorg. Chem. doi:10.1002/ejic.202101037 (c)2022 Wiley-VCH GmbH.

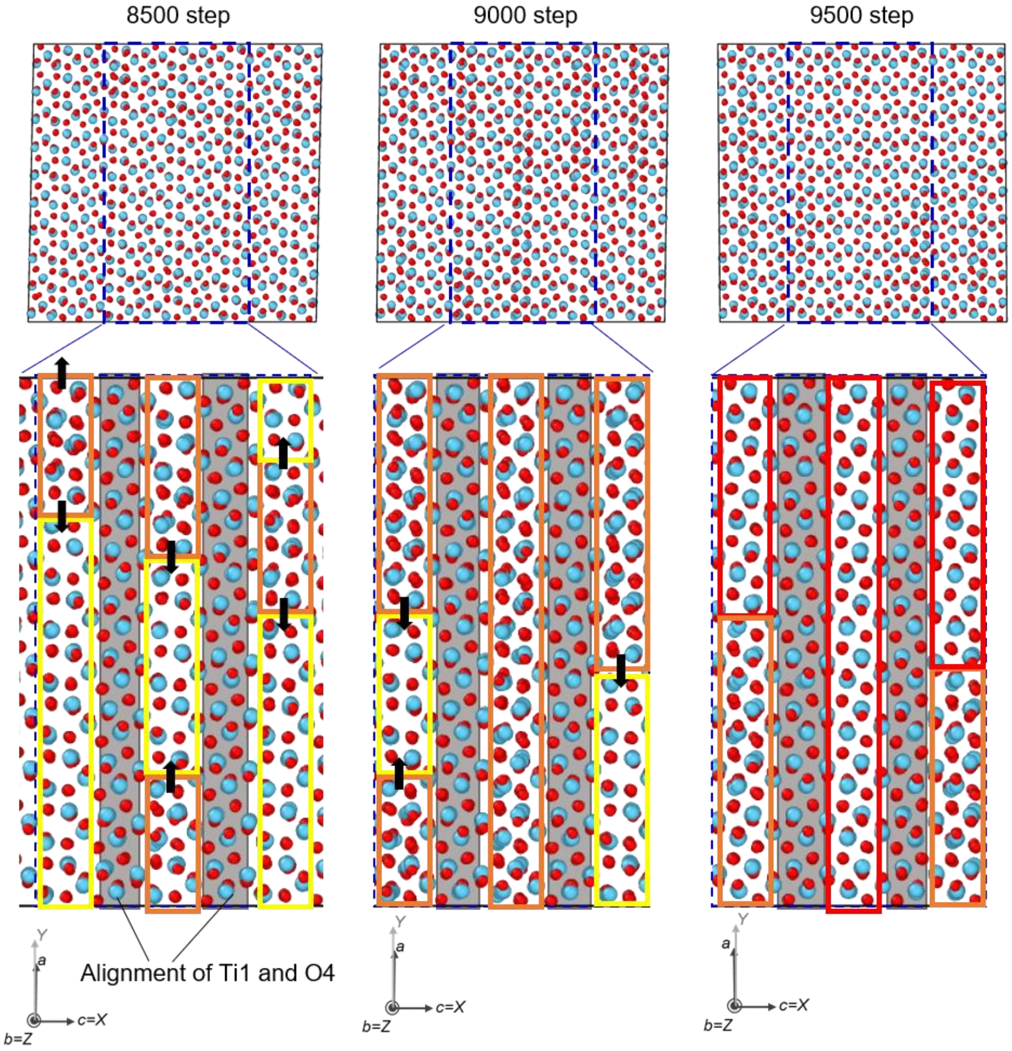

Figure 3.27 Phase transition propagation in a snapshot of 300 K, *X*-axis (*c*-axis) tensile stress ensemble, after 8500~9500 steps. Each snapshot is projected from the *ac*-plane, and 10 lattices are shown in the *b*-axis (perpendicular to a paper plane) direction. In each snapshot, an enlarged image of the area within the dashed line in the upper row (three periods in the *c*-axis direction) is shown in the lower row. The atoms in the yellow, orange, and red frames correspond to the orientation of the four-membered ring structure with Ti(3) and O(5) sites in the *a*-axis direction (top and bottom of the figure) in the intermediate state between the β- and λ-phases, the state in transition from the intermediate state to the λ-phase, and the state in transition to the λ-phase, respectively. The *a*-axis oriented rows of the four-membered ring structure consisting of Ti(1) and O(4) sites are shown in gray. The images were drawn by OVITO [88].

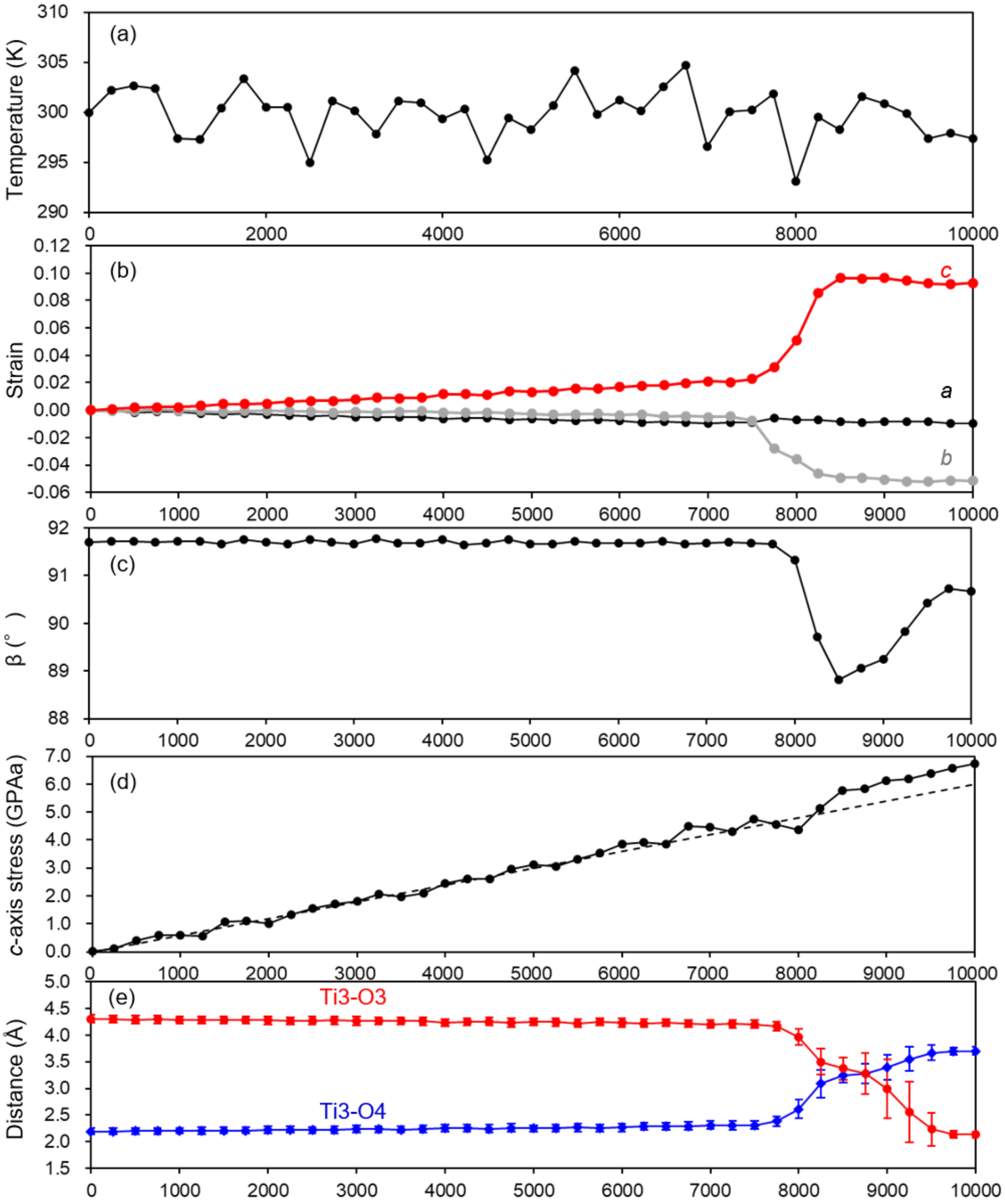

Figure 3.28 Plot of the physical properties of the tensile stress-inducing MD calculation on the *X*-axis (*c*-axis) direction at 300 K. (a) Measured temperature, (b) lattice strain, (c) β-angle, (d) measured stress component σ_{xx} in the *c*-axis (dashed line indicates control stress), and (e) site distances of Ti(3)-O(3) (in the same *ac*-plane) and Ti(3)-O(4) sites.

Reproduced with permission from T. Takeda, and S. Ohkoshi, Eur. J. Inorg. Chem. doi:10.1002/ejic.202101037 (c)2022 Wiley-VCH GmbH.

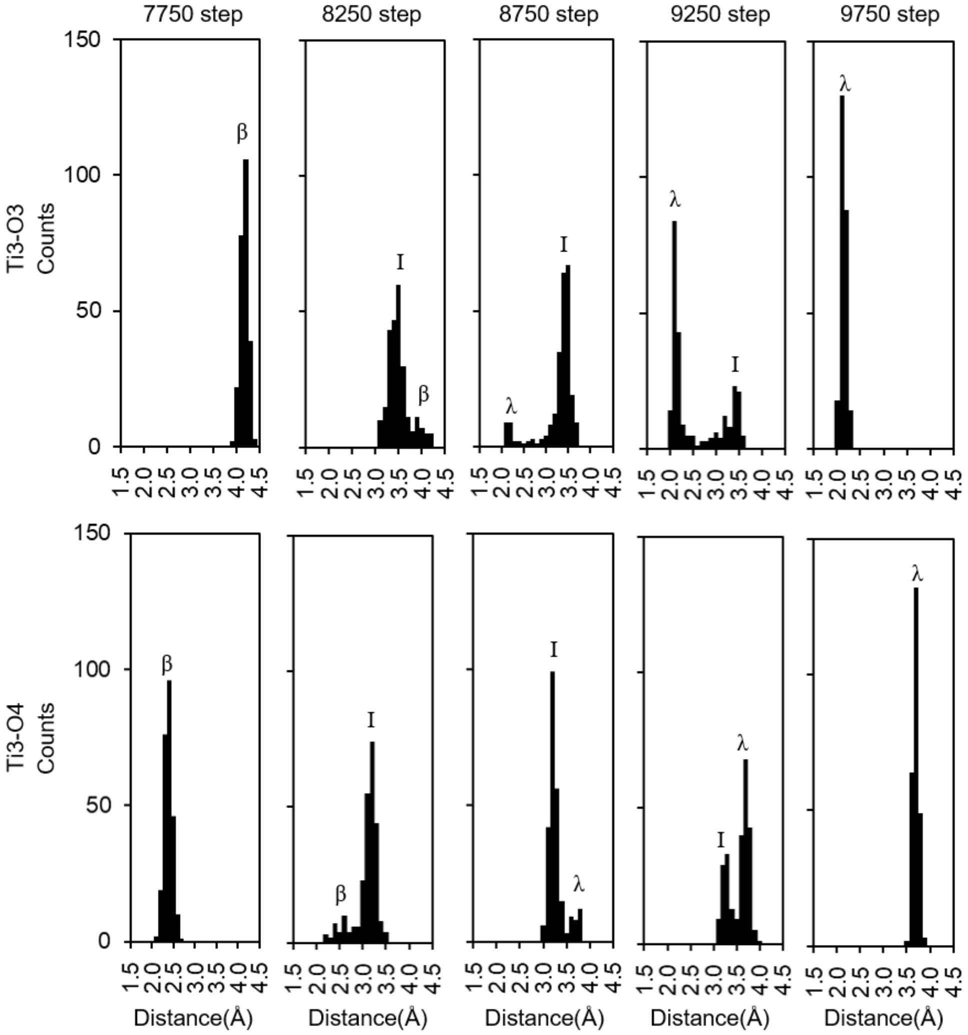

Figure 3.29 Distance between Ti(3)-O(3) (top) and Ti(3)-O(4) (bottom) sites from 7750 steps to 9750 steps during MD calculation of tensile stress inducing in *X*-axis (*c*-axis) direction at 300 K. For Ti(3)-O(3) sites, the distance between atoms in the same *ac*-plane (same *b*-axis=*Z*-axis components) is considered. For both inter-site distances, the distribution of the values sampled from two sites per cell and 500 sites in total in the supercell is shown. The peaks of the histogram show the β-phase, λ-phase, and Intermediate structures, which are intermediate between the two phases, with the symbols β, λ, and I, respectively.

Reproduced with permission from T. Takeda, and S. Ohkoshi, Eur. J. Inorg. Chem. doi:10.1002/ejic.202101037 (c)2022 Wiley-VCH GmbH.

第 3 章内 3.3.6 節に関する図版は雑誌等にて刊行予定のため、非公開とする。

Chapter 4 Conclusion for the research

In this thesis, the dynamic mechanism of the phase transition from β-phase Ti_3O_5 to λ-phase Ti_3O_5, which has not been discussed on a microscopic scale by theoretical calculations was discussed. The present approach can be applied to various phase transition phenomena in titanium dioxide and transition metal oxides with other compositions, and is expected to contribute to the investigation of their mechanisms.

Energy calculations on a lattice with uniaxial strain show the existence of a tensile stress-induced phase transition from the β- to λ-phase, which has not been found in either experimental or theoretical calculations. This value differs by one order of magnitude depending on the presence or absence of onsite Coulomb interaction, and the effective charges at the corresponding inequivalent sites in the β- and λ-phase differ, suggesting that the charge balance is involved in the phase transition and the stability of each phase.

The electronic structure calculations at various lattice constants indicate that the bond breaking around the inequivalent site Ti(3), which is necessary for the phase transition from λ-phase to the β phase, can be promoted by the phase reversal of the quantum orbitals due to the enhanced anisotropy in the *a*- to *c*-axis length ratio. Although the anisotropy of the pressure-induced phase transition from λ-phase to the β phase has not been fully discussed, it is expected that the phase transition can be controlled by anisotropic pressure or strain.

The soft-mode theory of structural phase transition was applied to β-phase Ti_3O_5 with uniaxial tensile strain on the *c*-axis, and the phonon mode dispersion was evaluated by the frozen phonon method. As the *c*-axis length increased, a significant softening was observed in the optical modes including the oscillations corresponding to the displacement directions of Ti(3) and O(5) sites in the phase transition to λ-phase. These results suggest that the vibrations corresponding to the displacement-type phase transition are destabilized in the tensile-strained β-phase, which can induce the phase transition.

Based on these results, the phase transition from β-phase Ti_3O_5 to λ-phase Ti_3O_5 with an elongated *c*-axis was actually observed by AIMD calculations with NVT ensemble. Visualization of the large displacement motion in the lattice of Ti(3) and O(5) sites and the change in the coordination structure during the phase transition from β-phase to λ-phase was successfully obtained. Furthermore, it was found that synchronous charge changes occur especially at Ti(2) and Ti(3) sites during the phase transition, suggesting that the charge transfer around these sites occurs together with the phase transition and is closely related to the phase transition.

In the NPT classical molecular dynamics calculations for a more realistic experimental system of a supercell under continuous tensile stress on the *c*-axis, a tensile stress-induced phase transition from β-phase to λ-phase was observed in the range of 5 GPa to 6 GPa. This calculation made successful simulation of a new stress-induced phase transition phenomenon, which has not been reported before, as expected from the existence of the isoenthalpy line in the strain-energy curve. The phase transition is classified into displacive phase transition around Ti(3) and O(5) sites, in the single unit cell, which corresponds to the one of NVT ensemble AIMD with fixed lattice constant. However, molecular dynamics with 8000 atoms revealed that there is a difference of emergence and propagation of phase transition in the direction of lattice, especially anisotropic against *a*-axis of the crystal lattice.

On the other hand, it was difficult to completely simulate the experimentally reported phase transition from β-phase to λ-phase or to the high-temperature monoclinic phase of similar structure by heating at atmospheric pressure. This might because that there are extra factors for successful simulation such as coordination structure in anomalous charge valence or time-revolution of charge on each timestep, which are limited in the potential function in this research. The phase transition between the β- and λ-phases is induced by a variety of external fields, such as heating, pressure, current, and laser light. To simulate those phenomena, further investigation, including improvement of potential performance and computational cost, is necessary for a more comprehensive analysis.

The main findings of this study are, firstly, that the phase transition phenomena in β-phase and λ-phase Ti_3O_5 can be simulated dynamically by theoretical calculations. By extending the computational conditions to include more diverse parameters, it will be possible to elucidate the microscopic mechanisms of the various phase transition phenomena that have been reported, or to discover and propose control of unknown phase transition phenomena. Secondly, a new stress-induced phase transition route was found in this study. In terms of applications, it may be possible to propose actuators, recording and switching devices by combining multiple external field-induced phase transitions. Furthermore, the synthesis of bulk-sized λ-phase Ti_3O_5, which has not been experimentally obtained so far, was shown to be possible by applying stress to β-phase Ti_3O_5, which is easy to obtain in bulk. So far, pure λ-phase Ti_3O_5 has been obtained only as powder or thin film, and the detailed physical properties are still under investigation. In addition, it is very important to synthesize a larger sample size for device applications. The experimental demonstration of the phase transition phenomenon in this study is expected to solve these problems by obtaining large-size λ-phase Ti_3O_5 samples experimentally.

Acknowledgements

I would like to express my heartfelt gratitude to Professor Ohkoshi for his guidance during the five years of my master's and doctoral course in conducting this research. I would like to express my sincere gratitude to Professor Ohkoshi for his kindness in accepting my request to enter the doctoral course again, even though there was a gap of three years after I completed the master's course. In addition, I would like to express my gratitude for your patience in discussing with me and guiding me to a constructive policy, which enabled me to write this academic paper despite the fact that I had no experience in this field. I was able to learn how to face an unknown research field.

I would like to express my gratitude to Associate Professor Asuka Namai, Assistant Professor Koji Nakabayashi, Project Assistant Professor Kosuke Nakagawa, Project Assistant Professor Kenta Imoto, Project Assistant Professor Marie Yoshikiyo, Project Assistant Professor Olaf Stefanczyk, and Professor Hiroko Tokoro at the University of Tsukuba for supporting me in an environment where I could proceed with my research without anxiety. Especially, I would like to express my gratitude to Assistant Professor Nakabayashi for his great support for my paper submission, and to Project Assistant Professor Yoshikiyo for providing me with various information on theoretical calculations.

I was encouraged by the students in the Ohkoshi and Tokoro laboratories for their positive attitude toward research, which kept the atmosphere of the laboratory intact despite the drastic changes in the world due to the disaster of COVID-19. In particular, I would like to take this opportunity to express my deepest gratitude to Mr. Ryota Shimoharai, who has often consulted with me about theoretical calculations and the handling of computers.

Finally, I would like to express my gratitude to my family for not only raising me, but also for interrupting my working life to devote myself to my studies for three years, and for supporting my family life.

References

[1] 固体の磁気的性質(固体物性シリーズ 6)、J. Grangle(著) 白鳥紀一、溝口正(訳)、丸善(1979).

[2] J. Valasek *Phys. Rev.* **17**, 475 (1921).

[3] W.J.Merz, *Phys. Rev.* **76**, 1221 (1949).

[4] P. Schwartz, *Phys. Rev. B* **4**, 920 (1971).

[5] T. Mehaddene, E. Kentzinger and B. Hennion, *Phys. Rev. B* **69**, 024304 (2004).

[6] G. Jaeger, *Arch. Hist. Exact. Sci.* **53**, 51 (1998).

[7] J. Tol'edano and P. Tol'edano, "The Landau theory of phase transitions", World Scientific (1987).

[8] S. Ohkoshi, Y. Tsunobuchi, T. Matsuda, K. Hashimoto, A. Namai, F. Hakoe and H. Tokoro, *Nat. Chem.* **2**, 539 (2010).

[9] S.Åsbrink and A. Magne'li, *Acta Cryst.* **12**, 575-581 (1959).

[10] K. Tanaka, T. Nasu, Y. Miyamoto, N. Ozaki, S. Tanaka, T. Nagata, F. Hakoe, M. Yoshikiyo, K. Nakagawa, Y. Umeta, K. Imoto, H. Tokoro, A. Namai and S. Ohkoshi, *Cryst.Growth Des.* **15**, 653-657 (2015).

[11] L. Pauling, *Zeitschrift für Kristallographie* **73**, 97 (1930).

[12] D. Velde, *Am. Mineral.* **60**, 566 (1975).

[13] F. Lang, L. Jowitt, D. Prabhakaran, R. D. Johnson, and S. J. Blundell, *Phys. Rev. B* **100**, 094401 (2019).

[14] T.Tohyamaa, R. Ogura, K. Yoshinaga, S. Naito, N. Miyakawa, and E. Kaneshita, *J. Phys. Chem. Solids* **127**, April 252 (2019).

[15] Z. Shen, Q. Shi, W. Huang, B. Huang, M. Wang, J. Cao, Y. Shi and T. Lu, *Appl. Phys. Lett.* **111**, 191902 (2017).

[16] U. Kolitsch and E. Tillmanns, *Acta. Cryst. E*, **59**, i36 (2003).

[17] Y. Nakamura, Y. Sakai, M. Azuma, and S. Ohkoshi, *Sci. Adv.* **6**, eaaz5264 (2020).

[18] M. Wang, W. Huang, Z. Shen, J. Gao, Y. Shi, T. Lu and Q. Shi, *J. Alloy and Compounds* **774**, 1189 (2019).

[19] W. Büssem, C. Schusterius and A. Ungewiss, *Ber. Deut. Keram. Ges.* **18** 433 (1937).

[20] Y. Suzuki and Y. Shinoda, Sci. Technol. *Adv. Mater.* **12**, 034301 (2011).

[21] I. E. Grey, C. Li and I. C. Madsem, *J. Solid State Chem.* **113**, 62 (1994)

[22] Hk. Müller-Buschbaum and H.-R. Freund, *Zeitschrift für Naturforschung B* **29**, 590 (1974).

[23] K. P. Anderson, A. K. Giri, R. P. Vinci and H. M. Chan, *J. Am. Ceram. Soc.* **102**, 5050 (2019).

[24] F. K. K. Kirshner, R. D. Johnson, F. Lang, d. D. Khalyavin, P. Manuel, T. Lancaster, D. Prabhakaran and S. J. Blundell, *Phys. Rev. B* **99**, 064403 (2019).

[25] G. Hyett, M. A. Green, and I. P. Parkin, *J. Am. Chem. Soc.* **129**, 15541 (2007).

[26] M. Onoda, *J. Solid State Chem.* **136**, 67 (1998).

[27] H. Tokoro, M. Yoshikiyo, K. Imoto, A. Namai, T. Nasu, K. Nakagawa, N. Ozaki, F. Hakoe, K. Tanaka, K. Chiba, R. Makiura, K. Prassides, and S. Ohkoshi, *Nat. Commun.* **6**, 7031 (2015).

[28] S. Ohkoshi, H. Tokoro, K. Nakagawa, M. Yoshikiyo, F. Jia, and A. Namai, *Sci. Rep.* **9**, 13203 (2019).

[29] R. Makiura, Y. Takabayashi, A. Fitch, and H. Tokoro, *Chem. An. Asian J.* **6**, 1886 (2011).

[30] K. Kobayashi, M. Taguchi, M. Kobata, K. Tanaka, H. Tokoro, H. Daimon, T. Okane, H. Yamagami, E. Ikenaga and S. Ohkoshi, *Phys. Rev. B* **98**, 085133 (2017).

[31] H. Chen, Y. Hirose, K. Nakagawa, K. Imoto, S. Ohkoshi and T. Hasegawa, *Appl. Phys. Lett.* **116**, 201904 (2020).

[32] K. Yoshimatsu and H. Kumigashira, doi:10.1021/acs.cgd.1c013214 (2021).

[33] R. Takahama, T. Ishii, D. Indo, M. Arizono, C. Terakura, Y. Tokura, N. Takashita, M. Noda, H. Kuwahara, T. Saiki, T. Katsufuji, R. Kajimoto, and T. OKuda, *Phys. Rev. Mater.* **4**, 074401 (2020).

[34] C. Mariette, M. Lorenc, H. Cailleau, E. Collet, L. Guérin, A. Volte, E. Trzop, R. Bertoni, X. Dong, B. Lépine, O. Hernandez, E. Janod, L. Cario, V. Ta Phuoc, S. Ohkoshi, H. Tokoro, L. Patthey, A. Babic, I. Usov, D. Ozerov, L. Sala, S. Ebner, P. Böhler, A. Keller, A. Oggenfuss, T. Zmofing, S. Redford, S. Vetter, R. Follath, P. Juranic, A. Schreiber, P. Beaud, V. Esposito, Y. Deng, G. Ingold, M. Chergui, G. F. Mancini, R. Mankowsky, C. Svetina, S. Zerdane, A. Mozzanica, A. Bosak, M. Wulff, M. Levantino, H. Lemke, and M. Cammarata, *Nat. Commun.* **12**, 1239 (2021).

[35] K. Umemoto, R. M. Wentzcovitch, D. J. Weinder and J. B. Parise, *Geophys. Res. Lett.* **33**, L15304 (2006).

[36] B. J. Alder and T. E. J. Wainwright, *J. Chem. Phys.* **31**, 459 (1959).

[37] A. Rahman, *Phys. Rev.* **136** (2A): A405 (1964).

[38] L. Verlet, *Phys. Rev.* **159**, 98 (1967).

[39] W. C. Swope, H. C. Andersen, P. H. Berens and K. R. Wilson. *J. Chem. Phys.* **76**, 637 (1982).

[40] S. Nos'e, *Molecul. Phys.* **100**, 191 (2002).

[41] S. Nos'e, *J. Chem. Phys.* **81**, 511 (1984).

[42] W. G. Hoover. *Phys. Rev. A* **31**, 1695 (1985).

[43] M. Parrinello and A. Rahman, *Phys. Rev. Lett.* **45**, 1196 (1980).

[44] R. Car and M. Parrinello, *Phys. Rev. Lett.* **55**, 2471(1985).

[45] J. Behler and M. Parrinello, *Phys. Rev. Lett.* **98**, 146401 (2007).

[46] R. Martoňák, D. Donadio, A. R. Oganoc and M. Parrinello, *Nat. Mater.* **5**, 623 (2006).

[47] A. Laio and M. Parrinello, *Proc. Nat. Acad. Sci. U.S.A.* **9**, 12562 (2002).

[48] M. Matsumoto, S. Saito and I. Ohmine, *Nature* **416**, 409 (2002).

[49] A. V. Verde, J. M. Acres, and J. K. Maranas, *Biomacromolecules*, **10**, 2118 (2009).

[50] F. Buda, G. L. Chiarotti, R. Car and M. Parrinello, *Phys. Rev. Lett.* **63**, 294 (1989).

[51] M. Levitt and A. Warshel, *Nature* **253**, 694-698 (1975).

[52] D. Plašienka, R. Martoňák, and M. C. Newton, *Phys. Rev. B* **96**, 054111 (2017).

[53] S. Wall, S. Yang, L. Vidas, M. Chollet, J. M. Glownia, M. Kozina, T. Katayama, T. Henighan, M. Jiang, T. A. miller, D. A. Reis, L. A. Boatner, O. Delaire, and M. Trigo, *Science* **362**, 572 (2018).

[54] S. E. Boulfelfel, D. Zahn, Y. Grin, and S. Leoni, *Phys. Rev. Lett.* **99**, 125505 (2007).

[55] T. Tsuchiya, T. Yamanaka and M. Matsui, *Phys. Chem. Mineral.* **25**, 94 (1998).

[56] Y. Akahama, M. Kobayashi and H. Kawamura, *Phys. Rev. B* **59**, 8520 (1999)

[57] Y. Oda, T. Tadano, R. Akashi, and S. Tsuneyuki, *Phys. Rev. Mater.* **3**, 033601 (2019).

[58] Y. Nagai, M. Okumura, K. Kobayashi and M. Shiga, *Phys. Rev. B* **102**, 041124(R) (2020).

[59] T. Tadano and S. Tsuneyuki, *J. Phys. Soc. Jpn.* **87**, 041015 (2018)

[60] P. Hänggi, P. Talkner and M. Borkovec, *Rev. Mod. Phys.* **62**, 251 (1990).

[61] K. Toyoura, Y. Koyama, A. Kuwabara, F. Oda and I. Tanaka, *Phys, Rev. B* **78**, 214303 (2008).

[62] G. Henkelman and H. J'onsson, *J. Chem. Phys.* **113**, 9978 (2000).

[63] F. Baletto, C. Mottet, and R. Ferrando, *Surf. Sci.* **446**, 31 (2000).

[64] S. Hara, S. Izumi, and S. Sakai, *J. Appl. Phys.* **106**, 093507 (2009).

[65] X. Fu, X. Hao, W. Chen, B. Yang, X. Zhao and L. Zuo, *J. Phys.: Condens. Matter*. **32**, 46LT01 (2020).

[66] A. Laio and M. Parrinello, *Proc. Natl. Acad. Sci. USA*, **99**, 12562 (2002).

[67] E. A. Carter, G. Ciccotti, J. T. Hynes, and R. Kapral, *Chem. Phys. Lett.* **156**, 472 (1989).

[68] W. Cochran, *Phys. Rev. Lett.* **3**, 412 (1959).

[69] H. Takahashi, *J. Phys. Soc. Jpn.* **16**, 1686 (1961).

[70] A. Einstein, *Annalen der Physik. Ser 4.* **327** 180 (1907).

[71] 濱口宏夫・平川暁子「ラマン分光法(日本分光学会測定法シリーズ 17)」、学会出版センター (1988).

[72] Y. Xie, H. -t. Yu, G. -x. Zhang and H.-g. Fu. *J. Phys.:Condens. Matter* **20**, 215215 (2008).

[73] K. -M. Ho, C. -L. Fu and B. N. Harmon, *Phys. Rev. B* **29**, 1575 (1984).

[74] K. Momma and F. Izumi, *J. Appl. Crystal.* **44**, 1272 (2011).

[75] T. Ozaki, *Phys. Rev. B* **67**, 155108, (2003).

[76] T. Ozaki and H. Kino, *Phys. Rev. B* **69**, 195113 (2004).

[77] T. Ozaki and H. Kino, *Phys. Rev. B* **72**, 045121 (2005).

[78] K. Lejaeghere *et al*., *Science* **351**, aad3000 (2016).

[79] R. Liu and J.-X. Shang, *Modelling Simul. Mater. Sci. Eng.* **20**, 035020 (2012).

[80] R. Liu, J. -X. Shang and F. H. Wang, *Comput. Mater.Sci.* **81**, 158 (2014).

[81] F. X.-Kai, C. W.-Qi, J.Z. Sheng, Y.Bo, Z. Xiang and Z. Liang, *Acta Physica Sinica* **68**, 207301 (2019).

[82] O. K. Orhan and D. D. O'Regan, *Phys. Rev. B* **101** 245137 (2020).

[83] J. P. Perdew, K. Burke, and M. Ernzerhof, *Phys. Rev. Lett.* **77**, 3865 (1996).

[84] S. L. Dudarev, G. A. botton, S. Y. Sarasov, C. J. Humphreys, and A. P. Sutton, *Phys. Rev. B* **57**, 1505 (1998).

[85] G. Henkelman, A. Arnaldsson, and H. J'onsson, *Comput. Mater. Sci.* **36**, 254 (2006).

[86] T. Tadano, Y. Gohda, and S. Tsuneyuki, *J. Phys.: Condens. Matter* **26**, 225402 (2014).

[87] A. Kokalj, *Comp. Mater. Sci.* **28**, 155 (2003).

[88] A. Stukowski, *Modelling Simul. Mater. Sci. Eng.* **18**, 015012 (2010).

[89] S. Plimpton, *J. Comp. Phys.* **117**, 1 (1995).

[90] J. Yu, S. B. Sinnott and S. R. Phillpot, *Phys. Rev. B* **75**, 085311 (2007).

[91] T.-R. Shan, B. D. Devine, T. W. Kemper, S. B. Sinnott, S. R. Phillpot, *Phys. Rev. B* **81**, 125328 (2010).

[92] T. Liang, T.-R. Shan, Y.-T. Cheng, B. D. Devine, M. Noordhoek, Y. Li, Z. Lu, S. R. Phillpot and S. B. Sinnott, *Mat. Sci. & Eng: R* **74**, 255-279 (2013).

[93] Y.-T. Cheng *et al.*, *J. Phys.: Condens. Matter* **26**, 315007 (2014).

[94] A. K. Rapp'e and W. A. Goddard III, *J. Phys. Chem.* **95**, 3358 (1991).

List of paper related to the thesis

(1) “Prediction of a tensile force–induced structural phase transition from β-Ti_3O_5 to λ-Ti_3O_5 by molecular dynamic simulations”
T. Takeda and S. Ohkoshi, *Eur. J. Inorg. Chem.* (2022), doi:10.1002/ejic.202101037

This paper corresponds to Chapter 3 in this thesis.